

InAs-Al Hybrid Devices Passing the Topological Gap Protocol

Microsoft Quantum[†]
(Dated: February 15, 2024)

We present measurements and simulations of semiconductor-superconductor heterostructure devices that are consistent with the observation of topological superconductivity and Majorana zero modes. The devices are fabricated from high-mobility two-dimensional electron gases in which quasi-one-dimensional wires are defined by electrostatic gates. These devices enable measurements of local and non-local transport properties and have been optimized via extensive simulations for robustness against non-uniformity and disorder. Our main result is that several devices, fabricated according to the design's engineering specifications, have passed the topological gap protocol defined in Pikulin *et al.* [arXiv:2103.12217]. This protocol is a stringent test composed of a sequence of three-terminal local and non-local transport measurements performed while varying the magnetic field, semiconductor electron density, and junction transparencies. Passing the protocol indicates a high probability of detection of a topological phase hosting Majorana zero modes. Our experimental results are consistent with a quantum phase transition into a topological superconducting phase that extends over several hundred millitesla in magnetic field and several millivolts in gate voltage, corresponding to approximately one hundred micro-electron-volts in Zeeman energy and chemical potential in the semiconducting wire. These regions feature a closing and re-opening of the bulk gap, with simultaneous zero-bias conductance peaks at *both* ends of the devices that withstand changes in the junction transparencies. The measured maximum topological gaps in our devices are 20-30 μeV . This demonstration is a prerequisite for experiments involving fusion and braiding of Majorana zero modes.

CONTENTS

1. Introduction	1	A. Electrostatic calibration from Hall bars	27
2. Topological gap device design and requirements	3	B. Simulated disorder realizations that fail the Topological Gap Protocol	28
2.1. Proximitized semiconductor nanowire model and its topological phase diagram	3	References	30
2.2. Gate-defined proximitized nanowire	4		
2.3. Material stack	5		
2.4. Phase diagram of ideal devices	6		
2.5. Disorder and uniformity requirements	7		
3. Topological gap protocol	8		
3.1. Overview	8		
3.2. Topological Gap Protocol applied to simulated data	11		
4. Experimental data	14		
4.1. Measurements of device A	14		
4.1.1. Topological Gap Protocol Stage 1	14		
4.1.2. Topological Gap Protocol Stage 2: Measurement A1	15		
4.1.3. Reproducibility of the data: Measurements A2 and A3	16		
4.2. Experimental data from other devices	21		
4.2.1. Additional devices B and C passing the Topological Gap Protocol	24		
4.2.2. Devices D and E <i>not</i> passing TGP	24		
5. Summary and discussion	24		
6. Looking ahead	27		
Acknowledgments	27		

1. INTRODUCTION

Topological quantum computation offers the promise of a high degree of intrinsic hardware-level fault-tolerance [1–6], potentially enabling a single-module quantum computing system that is capable of solving critical problems sufficiently rapidly to have societal impact [7]. This approach hinges on (a) reliably producing a stable topological phase of matter that supports non-Abelian quasiparticles or defects and (b) processing quantum information through protected operations, such as braiding. The former is challenging due to the material parameter and disorder requirements for topological phases of matter. In this paper, we report on three-terminal devices that pass the stringent topological gap protocol [8] and therefore satisfy these requirements. We further extract the gap associated with the topological superconducting phase in our semiconductor-superconductor nanowire devices [9–12].

Topological phases are a form of matter in which the ground state has long-range quantum entanglement and there is a gap to excited states [13]. Unlike phases of matter that can be distinguished completely by local measurements, topological phases are identified by the transformations of their low-energy states that result from fusing and braiding their quasiparticles and defects. Directly measuring these properties in experiments is rather

subtle [14], hindering efforts to fully determine the topological order of candidate materials. In the fractional quantum Hall regime, for example, a quantized Hall conductance reveals the presence of a non-trivial topological phase, but many different topological phases can have the same Hall conductance. Consequently, different measurements are necessary to determine which topological phase is present in a given device [15–22].

In the case of quasi-one-dimensional superconducting wires without any symmetries enforced, there are only two phases — one trivial and one topological. The latter supports Majorana zero modes (MZMs) localized at the ends of the nanowire [9, 11, 12]. While MZMs can be directly detected through fusion and braiding, one of their auxiliary signatures are zero-bias peaks (ZBPs) in the differential tunneling conductance at the nanowire’s ends [23–28]. Indeed, most of the earlier experimental studies of candidate topological superconductors focused on ZBPs [29–42]. However, ZBPs can also be caused by disorder [43–45], smooth potential variations near the tunnel junction [46–50], unintentional quantum dots [51, 52], or a supercurrent [53]. These trivial ZBPs can persist over a fairly large range of system parameters [54–56].

A ZBP associated with an MZM must have a partner at the other end of the wire and should be stable to variations in the electric and magnetic fields in the device. The stability of MZMs with respect to such variations is determined by the bulk gap. However, if a device has a sufficiently large number of control parameters, it is likely that it can be tuned into a configuration in which it has trivial ZBPs at both ends. Meanwhile, the predicted range of stability of a topological phase depends strongly on device geometry, the full stack of materials, and disorder, rendering it difficult to distinguish “stable” ZBPs from “accidental” ones purely empirically. Analyzing the detailed shapes of tunneling conductance spectra leads to some loose qualitative patterns, but there is no sharp binary distinction between the local tunneling conductance spectra associated with MZMs and trivial ZBPs at non-zero temperature. In short, neither more extensive data sets of ZBPs nor more beautiful ZBPs can distinguish the topological and trivial phases. Therefore, it is crucial to develop a practical, reliable protocol that enables the detection of the topological superconducting phase of a nanowire, and it is clear that additional measurements beyond the tunneling conductance are necessary for such a protocol.

This challenge is addressed by the topological gap protocol (TGP) [8], which is designed to reliably identify the topological phase through a series of stringent experimental tests. At the heart of this protocol is the fact that there is necessarily a quantum phase transition between the trivial and topological phases [57]. The protocol detects a bulk phase transition between low-magnetic-field and high-magnetic-field phases via a bulk gap closing. It establishes that the high-field phase is topological through the stability of its ZBPs, in a manner that

we specify below. The TGP requires three-terminal device geometries, which overcome the limitations of many earlier two-terminal devices. They allow ZBPs to be simultaneously observed at both ends and also allow for a measurement of the bulk transport gap through the *non-local conductance*. The protocol is passed when (a) ZBPs are observed in the local conductances measured at tunnel junctions at both ends of a wire, and they are stable to changes in the junction transparency; (b) these stable ZBPs persist over a range of magnetic fields and electron densities in the wire; (c) a closing and re-opening of the bulk transport gap is detected in the non-local conductances; (d) there is a region in the bulk phase diagram whose boundary is gapless and whose interior is gapped and has stable ZBPs; (e) the observed bulk transport gap throughout this region — the *topological gap* — exceeds the resolution of the measurement.

The protocol has been validated through extensive simulations. The purpose of these simulations is *not* to establish qualitative similarities between simulated and measured data. The purpose of these simulations is to test the TGP on simulated devices in which we can compare the results of the TGP with a topological invariant. We find that the protocol is able, with high probability, to distinguish MZMs from trivial Andreev bound states and to determine whether topological superconductivity is present in the parameter range scanned in a data set. Having thus confirmed the reliability of the TGP on simulated data, we formulate the central question of this paper: *are there devices that pass the TGP?*

In this paper, we answer this question in the affirmative by presenting data from three devices, named A, B, and C, that have passed this protocol with respective maximum topological gaps ranging between 20–30 μeV . As we explain in more detail in Sec. 2, our devices are based on heterostructures combining indium arsenide (InAs) and aluminum (Al). The superconducting component is an Al strip, epitaxially-grown on the semiconductor so that it induces superconductivity via the proximity effect. The semiconducting portion is a shallow InAs quantum well hosting a two-dimensional electron gas (2DEG) that has been depleted by electrostatic gates, except for a narrow conducting wire that remains underneath the aluminum strip. Within this suite of components, we have optimized both the material stack and the device geometry through simulations in which many different device parameters were varied in order to find device designs with the largest topological gap, given currently achievable levels of disorder and uniformity. Many of the specifications are quite demanding, including: (1) higher mobility ($> 60,000 \text{ cm}^2/\text{Vs}$) than previously achieved in shallow InAs quantum wells and (2) gate-defined wires that are sufficiently narrow ($< 120 \text{ nm}$) as to enable tuning into the single sub-band regime.

Our simulations demonstrate that disorder is the principal obstacle to realizing a topological phase supporting MZMs. These simulations include self-consistent electrostatics, the orbital effects of the magnetic field,

and realistic semiconductor-superconductor coupling; see Refs. [41, 58, 59] for more details. Consequently, they show both qualitatively and quantitatively how device design can impact the effective disorder strength. Both simulations and fabrication are governed by the same device design file, so our fabricated devices can be directly compared to simulated devices. We thereby determined the target disorder levels for fabricated devices such as devices A-C.

Our simulations indicate that mesoscopic fluctuations are important. At currently-achievable disorder levels, even devices with the same average disorder level can have different TGP outcomes: some disorder realizations will pass while others fail. In other words, the disorder strength determines an expected yield for passing the TGP which goes to zero above a critical value but is between 0% and 100% over a range of disorder levels. As expected from these simulation results, we have also measured devices that were very similar to devices A-C but did not pass the TGP, and we report on data from two of them, which have been named devices D and E.

As noted above, the hallmarks of most topological phases, including the one discussed here, are rather subtle: there is no signature as immediate as a quantized conductance or Meissner effect. Instead, the existence of a topological phase is imprinted on the measurable properties of the system in a manner that can only be identified through an elaborate measurement and analysis procedure such as the TGP or the even more elaborate procedures necessary for fusion and braiding. Thus, it is of paramount importance that the TGP has been validated by applying it to simulated transport data and comparing the results with a topological invariant. Out of 61 different simulated disorder realizations¹ of varying disorder levels, there were no instances of a “false positive” TGP outcome in which a device passed the TGP but did not have a topological phase. Hence, we expect a false positive ratio of no more than $(\ln 2)/61$ for the TGP, thus concluding that devices A, B, and C have a probability $> 98\%$ of being in the topological phase. To the best of our knowledge, these devices are the first to have passed as stringent a set of requirements as those encompassed by the TGP, namely (a) concurrent ZBPs that are stable both with respect to changes of the junction parameters and also with respect to changes of the bulk parameters that are larger (in appropriate units) than the bulk gap; and (b) a bulk gap closing and re-opening in response to an increasing magnetic field that is visible in the non-local conductance, indicating a quantum phase transition into a phase with correlated ZBPs.

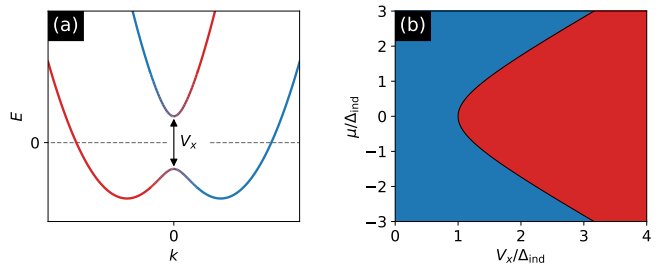


FIG. 1. (a) Energy spectrum as a function of momentum k along the nanowire. Rashba spin-orbit coupling splits the parabola at the bottom of the band into two parabolas displaced in k . The Zeeman energy V_x is proportional to the external magnetic field perpendicular to the direction of the Rashba spin-orbit coupling. A non-zero Zeeman energy V_x opens a gap at $k = 0$. When the chemical potential μ is within the gap, the nanowire Hamiltonian Eq. (1) has only one pair of Fermi points with spin and momentum locked. The color gradient represents the change of spin orientation with momentum. (b) The topological phase diagram as a function of Zeeman energy V_x and chemical potential μ . Δ_{ind} is the superconducting gap induced in the semiconductor nanowire. The low-field (blue) phase is a trivial superconductor while the high-field (red) phase is a topological superconductor that supports MZMs at the opposite ends of the nanowire.

2. TOPOLOGICAL GAP DEVICE DESIGN AND REQUIREMENTS

2.1. Proximitized semiconductor nanowire model and its topological phase diagram

In this section we briefly review the proximitized nanowire model [11, 12] which supports topological superconductivity over a range of densities and magnetic fields. The minimal model is comprised of a semiconductor nanowire with Rashba spin-orbit interaction coupled to a conventional (s -wave) superconductor. The effective Hamiltonian for such a system is:

$$H = H_{\text{SM}} + H_{\text{SC}}, \quad (1)$$

$$H_{\text{SM}} = \int_0^L dx \psi_{\sigma}^{\dagger}(x) \left(-\frac{\partial_x^2}{2m^*} - \mu + i\alpha \hat{\sigma}_y \partial_x + V_x \hat{\sigma}_x \right) \psi_{\sigma}(x),$$

$$H_{\text{SC}} = \int_0^L dx (\Delta_{\text{ind}} \psi_{\uparrow}^{\dagger}(x) \psi_{\downarrow}^{\dagger}(x) + \text{h.c.}).$$

Here, “SM” and “SC” are abbreviations for, respectively, semiconductor and superconductor, m^* , μ and α are the effective mass, chemical potential, and Rashba spin-orbit coupling, respectively. V_x is the Zeeman splitting due to the applied magnetic field B along the nanowire: $V_x = g_{\text{SM}} \mu_B B / 2$, where g_{SM} and μ_B are, respectively, the Landé g -factor and Bohr magneton. The proximity to the s -wave superconductor is effectively described by the Hamiltonian H_{SC} in which Δ_{ind} is the induced pairing potential.

¹ We had a number of disorder realizations in which the junctions didn’t pinch off, leaving us with 61 on which the TGP could be run.

The zero-temperature phase diagram of the nanowire Hamiltonian of Eq. (1) consists of a trivial (s -wave-like) phase and a topological phase, as shown in Fig. 1. The latter supports MZMs at the opposite ends of the nanowire and is in the same phase as a spinless p -wave superconductor [9]. The trivial and topological phases are separated by a quantum phase transition at $V_x = \sqrt{\mu^2 + |\Delta_{\text{ind}}|^2}$ which is necessarily accompanied by the closing of the bulk gap. The stability of a topological phase is characterized by its bulk transport gap or, equivalently, the gap to extended excited states, which we call the topological gap.² In the idealized case of Eq. (1), this is simply the bulk gap. The corresponding two-dimensional topological superconducting state can occur in $p + ip$ superconductors [57], at the surface of a topological insulator [60, 61], in ferromagnetic insulator-semiconductor-superconductor heterostructures [10, 62–66], and in s -wave superfluids of ultra-cold fermionic atoms [67, 68].

This model neglects many of the ingredients of real devices, such as disorder, additional sub-bands, and the orbital effect of the magnetic field. To address this, we have developed realistic 3D simulations that take these effects into account. These simulations include self-consistent electrostatics, orbital magnetic field contributions, realistic semiconductor-superconductor coupling [58, 59, 69–72]. We have validated these simulations through comparison with ARPES [73], THz spectroscopy [74], the Hall bar measurements reported in Appendix A, and transport through multiple types of previous devices involving proximitized semiconductor nanowires [41, 75–77]. We also take into account multiple disorder mechanisms such as charged disorder and variations of geometry and composition along the wire length, as discussed in Sec. 2.5. The superconductor’s degrees of freedom are integrated out, yielding a formulation in which it is encapsulated by self-energy boundary conditions [41, 76, 77]. Using this advanced simulation model, we optimized the design for gate-defined devices based on high-quality 2DEG heterostructures in order to minimize the effects of disorder, additional sub-bands, and the orbital effect of the magnetic field, thereby realizing the physics encapsulated in Eq. (1).

2.2. Gate-defined proximitized nanowire

Our devices are defined by an Al strip separated from an InAs quantum well by a barrier layer. A cross-section of the device, dubbed a “topological gap device,” is shown in Fig. 2(d), where the Al strip is light grey. The strip’s dimensions have been optimized using the advanced simulations described above: length $10\ \mu\text{m}$, width

$< 120\ \text{nm}$, thickness $< 10\ \text{nm}$. The length is in the direction perpendicular to the cross-section in Fig. 2(d). The Al strip is covered by a 2 nm thick top oxide formed by controlled oxidation [not shown in Fig. 2(d)]. The Al strip features larger Al pads at each end of its $10\ \mu\text{m}$ length, which can be seen at the right and left edges of the scanning electron micrograph (SEM) image in Fig. 2(b). The pads are contacted with Ti/Au Ohmic leads, by which the Al strip is grounded. We will denote the direction perpendicular to the surface of the quantum well as the z -direction, while the directions along and perpendicular to the Al strip are the x - and y -direction, respectively, as shown in Fig. 2(c,d).

There is a dielectric layer that separates the superconductor-semiconductor heterostructure from the electrostatic gates that are at the top of the cross-section in Fig. 2(d). The gates deplete the 2DEG except underneath the Al, which partially screens their electric fields, thereby creating a high-quality nanowire. The top view in Fig. 2(a) and the SEM image in Fig. 2(b) show that this split-gate structure is divided into three sections: three plunger gates and three cutter gates. The three plunger gates serve to deplete the 2DEG on their side of the Al strip while the three cutter gates deplete the 2DEG on the other side. Once the 2DEG has been depleted, operating the plunger gates at even more negative voltages tunes the electrochemical potential and, therefore, the density underneath the Al by the fringe electric fields that remain after screening by the Al. The densities in the left, middle, and right sections can be controlled independently by the three plunger gates. We operate in the low-density limit in which only the lowest z -direction sub-band is occupied so, here and henceforth, will use the term “sub-band” for y -direction sub-bands. The left and right plungers control the densities underneath the corresponding sections of the Al, which are normally set for full depletion (no occupied sub-bands) underneath the Al. The width of the Al strip was chosen to enable this for moderate gate voltages $V_{\text{dep}} > -3\ \text{V}$ and also to minimize the orbital effects of a magnetic field in the x -direction.

There are two side tunnel junctions at the boundaries between the middle cutter gate and the left/right cutter gates, enabling the 3-terminal measurements [78–82] of the conductance matrix that are necessary for the TGP, as we discuss in Sec. 3.1. In addition to depleting the 2DEG on the opposite side of the Al strip from the plungers, the left and right cutter gate voltages V_{lc} and V_{rc} are also used to vary, respectively, the transparency of the left and right tunnel junctions. The split-gate geometry with plunger-cutter pairs ensures independent tuning of density and junction transparency for each section of the gate-defined nanowire. The two junctions are typically tuned into the tunneling regime in which the above-gap low-temperature differential tunneling conductance is $\lesssim e^2/h$, while the Al strip is grounded. The junctions are connected via conducting paths in the 2DEG to Ohmic contacts. There are two “helper” gates, which

² Note that even the states above the observed transport gap are expected to be localized in a sufficiently long system.

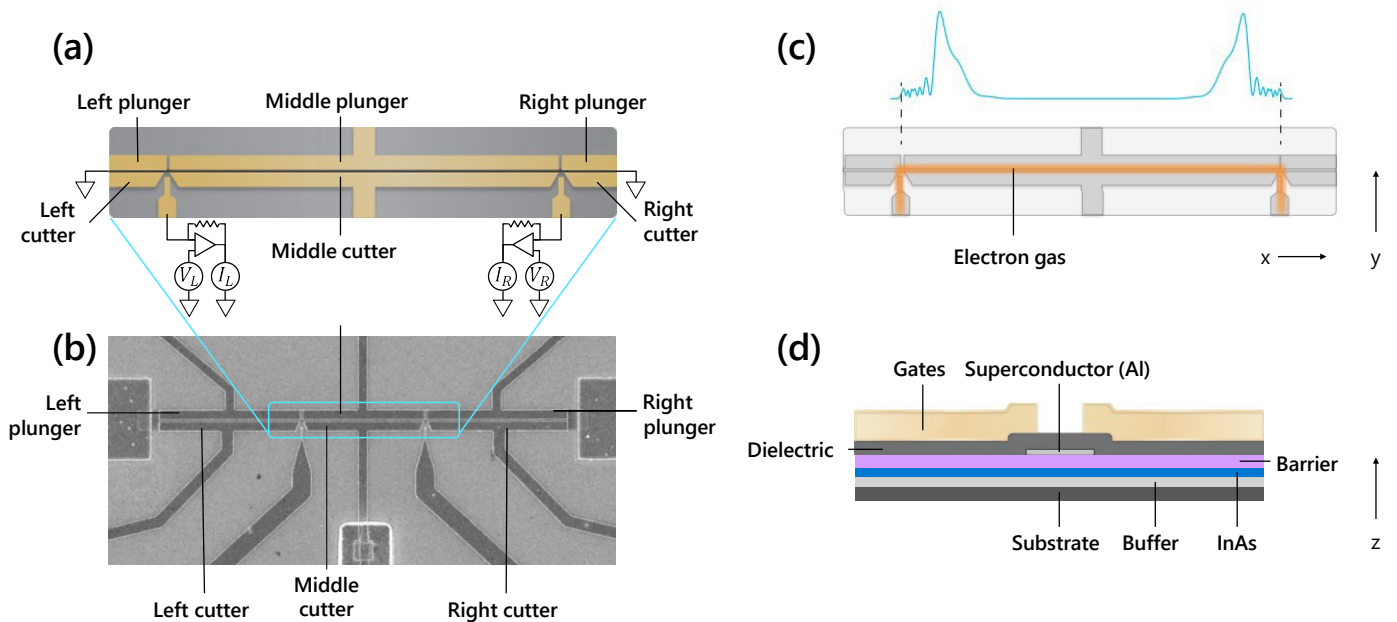


FIG. 2. (a) A schematic of the top view of the active area of a topological gap device. All of the labelled gates serve to deplete the 2DEG in the InAs quantum well to define a high-quality one-dimensional conducting channel. The left, middle, and right plungers also tune the density in the corresponding sections of the device, while the left and right cutters also open and close the junctions. The two unlabelled gates are the “helper gates” which are used to increase the electron density in the junctions and leads, the latter of which are connected to a measurement circuit as shown in this panel. (b) An SEM image of a topological gap device. The blue line indicates the active region depicted in (a). (c) Region of non-zero electron density (orange) in the InAs quantum well when the device is tuned to the operating regime: the middle section (underneath the middle cutter/plunger) is tuned to the topological regime while the outer sections (underneath the left/right cutter/plunger gates) are tuned to the trivial phase using the plunger gates. The blue curve shows the local density of states in the wire near zero energy, computed in the ideal disorder-free limit. (d) A schematic of the cross-section of a topological gap device, in which the Al strip induces proximity superconductivity in the one-dimensional InAs nanowire that is defined by the gates shown in panel (a) and extends perpendicular to this cross-sectional view. The x -, y -, and z -directions are indicated in panels (c,d).

are the unlabelled gates at the bottom of Fig. 2(a); they extend from the junctions to the bottom edge of the SEM in Fig. 2(b). The helper gates define these conducting paths by accumulating carrier density in the 2DEG underneath them and keeping it conductive. The orange region in Fig. 2(c) shows where the electron density is non-zero in the 2DEG in the device’s normal operating regime: underneath the middle section of the Al strip and underneath the helper gates.

We will call the semiconductor underneath the middle section “the wire,” and the superconducting gap that is induced in the wire via the proximity effect the “induced gap” Δ_{ind} . We denote the middle plunger gate voltage by V_p , which tunes the density in the wire. At the optimal operation point, the wire is tuned to the single-sub-band regime that occurs just before full depletion $V_p \gtrsim V_{\text{dep}}$. We will focus on the phase diagram of the wire as a function of the middle plunger gate voltage V_p and the magnetic field B .

The wire must be several times longer than the coherence length in the superconducting state induced in the wire in order for us to conclude that ZBPs observed at the two junctions are due to two different states, one at each

junction [the situation depicted in Fig. 2(c)], rather than the exponential tails of a single state [83]. In our simulations, the disordered coherence length in the topological phase is $< 1 \mu\text{m}$, so the wire is designed to be at least $3 \mu\text{m}$. This also ensures that observed transport gap closings are a signal that there is a non-zero density of states in the bulk at zero energy which have non-vanishing matrix elements to both leads [80]. On the other hand, the wire cannot be too long since the visibility of gap closings will be strongly suppressed if the length of the wire is more than several times the localization length [78]. The outer sections (underneath the left/right cutter/plunger gates) must be significantly longer than their superconducting coherence lengths in order to prevent quasiparticle transport below the parent gap at full depletion. For this reason, they are designed to be longer than $3 \mu\text{m}$.

2.3. Material stack

The material stack of the topological gap device is optimized to produce a large topological gap. To achieve a topological phase, the semiconductor stack needs to

produce a large spin-orbit coupling and a large nominal g -factor in the confined 2DEG. In addition, the heterostructure should provide a low disorder environment, typically parameterized by high 2DEG mobility at low temperatures. Given the lack of suitable insulating and lattice-matched substrates, the active region is grown on an InP substrate employing a graded buffer layer to accommodate lattice mismatch.

The active region consists of the Al superconductor, an upper barrier, the InAs quantum well, and the buffer. The upper barrier layer plays a critical role in fine-tuning the coupling between the superconductor and the 2DEG residing in the quantum well. To drive the device into the topological phase, B needs to be increased until the Zeeman energy $\mu_B |g^*| B/2$ exceeds the induced gap Δ_{ind} with $|g^*|$ being the renormalized g -factor in the superconductor-semiconductor heterostructure. For strong coupling between the wire and the Al strip, Δ_{ind} would approach the gap in the Al strip Δ_{Al} and the electronic wavefunction of the single occupied sub-band of the wire would have large weight in the Al strip. In this case, the nominal g -factor would be renormalized to small values (since the g -factor of Al is small and positive while the g -factor of InAs is large and negative). In such a case, $\mu_B |g^*| B/2$ wouldn't approach Δ_{ind} until the magnetic field is very large (> 2.5 T), close to the critical in-plane field of the Al strip [27, 58, 84, 85]. Conversely, if the coupling between the superconductor and semiconductor were too weak, the maximum attainable topological gap would be small, since it is bounded by Δ_{ind} . Hence, the material stack must satisfy $k_B T \ll \Delta_{\text{ind}} \ll \Delta_{\text{Al}}$. As we shall see in Sec. 4.1, the parent gap in the Al strip is $\Delta_{\text{Al}} \approx 300 \mu\text{eV}$ (this is strongly dependent on the Al thickness). For an optimized heterostructure, according to our simulations of the device of Fig. 2(a), we expect $100 \mu\text{eV} < \Delta_{\text{ind}} < 200 \mu\text{eV}$, corresponding to an induced gap to parent gap ratio of $0.33 < \Delta_{\text{ind}}/\Delta_{\text{Al}} < 0.67$, and $4 < |g^*| < 7$.

Another function of the upper barrier layer is to separate the quantum well states from disorder on the dielectric-covered surface of the stack, thus enhancing the electron mobility. The quantum well thickness is chosen to minimize orbital effects from the magnetic field applied in the x -direction, to allow electrostatic tuning, and to retain the desirable properties of InAs, including optimally renormalized g^* .

Rashba spin-orbit coupling in the wire, characterized by the parameter α , enables superconductivity to co-exist with the magnetic field B . Although α does not determine the critical field for the transition into the topological phase, it does contribute to the size of the topological gap and the extent of the topological phase in parameter space. The heterostructure has been engineered to have spin-orbit coupling in the range of 5 to 15 meV · nm. In the simulations presented in this paper, we take $\alpha = 13 \text{ meV} \cdot \text{nm}$.

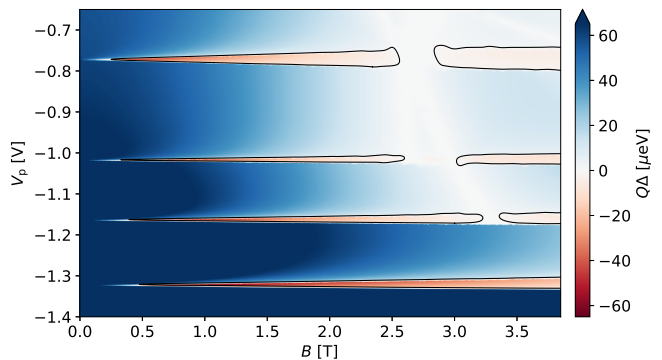


FIG. 3. The simulated phase diagram of the device design of Sec. 2.2 and the material stack of Sec. 2.3 in the ideal disorder-free limit. Here, $Q = +1$ in the trivial phase and $Q = -1$ in the topological phase. Hence, the color scale indicates the size of the gap in the trivial (blue) and topological (red) phases. The black curves indicate the phase transition where the topological invariant changes sign. The axes B and V_p , the magnetic field and plunger gate voltage, respectively, are the actual control parameters of the device. Most of the phase diagrams in this paper will similarly be in the (B, V_p) plane. This phase diagram is for a wire of infinite length. The maximum topological gap in the lowest sub-band is approximately $60 \mu\text{eV}$.

2.4. Phase diagram of ideal devices

For the device design described in Sec. 2.2 and the material stack described in Sec. 2.3, we have computed the phase diagram in the ideal disorder-free limit as a function of the actual control parameters of the device, V_p and B . [This is to be contrasted with Eq. (1) and Fig. 1, which contain the effective parameters μ and V_x .] The red parabola in Fig. 1 has now become a sequence of red slivers in the ideal phase diagram in Fig. 3. Darker red corresponds to larger topological gap and darker blue corresponds to larger trivial superconducting gap, as indicated by the color scale on the right-hand-side of the figure. The red slivers are topological phases with different numbers of occupied 1D sub-bands in the wire [86]. When we zoom in on any one of these slivers, we see that it has the parabolic lobe-like shape $|g^*| \mu_B B/2 > \sqrt{\mu^2 + \Delta_{\text{ind}}^2}$ that follows from Eq. (1). Here, the single-sub-band topological phase is at $V_p \sim -1.35$ V, and it has a larger topological gap than when there are more occupied sub-bands. Recall that one of the design criteria was that the single-sub-band regime could be reached for moderate gate voltages; this figure confirms that it is satisfied by this design. As we increase V_p , thereby increasing the number of occupied sub-bands, the effective cross-sectional area of the gate-defined nanowire increases and, at some point, the orbital effect of the applied magnetic field becomes very important. The characteristic orbital-field-induced gap closing is visible at $B \sim 3$ T and $V_p \gtrsim -1.2$ V. Thus, in order to maximize both the accessible volume of the topological phase and its maximum gap, it is necessary to tune the

device into the single-sub-band regime. In this regime, the disorder-free limit of the device depicted in Fig. 2 is well-represented by the Hamiltonian (1).

2.5. Disorder and uniformity requirements

Unlike in Fig. 3, real devices have disorder, which suppresses the topological phase. There are design-dependent limitations on the degree of imperfection that our devices tolerate [87–97]. Even small local variations in any of a number of device parameters can cause significant variations in the potential experienced by the electrons along the wire, causing significant changes to the phase diagram of Fig. 3. For weak disorder, this leads to a decrease of the topological gap and an increase of the disordered superconducting coherence length in the topological phase. As the disorder strength is increased, these variations can create small non-topological regions in the otherwise topological wire, thus nucleating additional subgap states at the domain walls. Eventually these subgap states hybridize and lead to the breakdown of the topological phase through Griffiths’ effects [87]. In the limit in which the clean topological gap Δ_{T} is small, the stability condition for the topological phase is $\ell_c > \xi_{\text{T}}$ [90], where ℓ_c is the localization length in the normal state (which in one dimension is equal to twice the mean free path for short-range disorder [98]) and ξ_{T} is the coherence length in the clean topological superconductor. Equivalently, this can be rephrased in terms of energy scales as $\Delta_{\text{T}}\tau > \hbar/2$, where τ is the elastic scattering time. The precise location of the disorder-driven phase transition is more complicated when the clean topological gap is not much smaller than the Fermi energy [93]. Note that, in a finite-sized system, this transition will become rounded. Consequently, a topological phase can be found in some percentage of devices (which we call the “yield”) for average disorder levels that would destroy the topological phase in the thermodynamic limit.

In our devices, there are many different sources of disorder, ranging from geometric disorder to charged disorder [27, 38, 99]. Most disorder mechanisms can be characterized by the quenched Gaussian disorder model [100] defined by the variance δV^2 and spatial correlation length κ of the random potential $V(x)$. We find that the dominant disorder mechanisms can be approximately described by the second-order cumulant defined below in Eq. (2). The impact that each disorder source has on the mean free path is highly dependent on the specific design, and the design in Fig. 2(a) has been optimized to be as forgiving as possible. In the low-density (i.e. single sub-band) regime in which we operate, charged disorder dominates scattering [101]. From an analysis of the density-dependence of the mobility of Hall bars, we conclude that charged disorder is located primarily at the interface between the semiconductor surface and the gate dielectric. Hall bar measurements allow us to extract the average density of charged imperfections at

the semiconductor-dielectric interface and the lever arm, which is the derivative of the chemical potential in the wire with respect to the applied gate voltage. This is illustrated in Appendix A. Each chip studied in this paper has both topological gap devices and Hall bars, enabling us to extract the average density of charged imperfections for each chip and to assess the impact on topological gap devices of chip-to-chip changes in the disorder level. We similarly extract other relevant disorder parameters from measurements and use them in our simulations of topological gap devices.

We project the disorder into an effective model, where it is described by a disorder potential $V(x)$ with a characteristic correlation function

$$\langle V(x)V(x') \rangle = \delta V^2 \exp(-|x - x'|/\kappa), \quad (2)$$

where both the strength of disorder δV and its correlation length κ depend on the density of charged imperfections as well as the device design. In this effective model, the scattering rate due to charged imperfections can be evaluated to lowest order in δV :

$$\frac{\hbar}{\tau} = \frac{\delta V^2}{2E_{\text{F}}} \frac{2k_{\text{F}}\kappa}{1 + (2k_{\text{F}}\kappa)^2}. \quad (3)$$

Here, E_{F} and k_{F} are the Fermi energy and momentum. The Fermi wavelength in the relevant (single sub-band) density regime is typically $k_{\text{F}}^{-1} \simeq 30 - 80$ nm; the charge disorder correlation length $\kappa \approx 75 - 100$ nm. Due to the semiconductor’s small Fermi energy, the requirements on the disorder strength are stringent. Disorder sources with correlation lengths $\kappa \gtrsim k_{\text{F}}^{-1}$ are especially deleterious, and a careful treatment of these types of disorder must take higher-order corrections to the scattering time into account [101].

We have optimized the device geometry with respect to charged imperfections at the semiconductor-dielectric interface by choosing the Al width as wide as possible while still maintaining the ability to tune into the single sub-band regime, so that the active region in the InAs quantum well is as far as possible from charged disorder at the interface between semiconductor and dielectric [see Fig. 2(d)]. By performing self-consistent simulations [58, 59], we find the disorder potential underneath the Al. We use this to estimate the maximum possible average density of charged impurities that the topological phase can tolerate in the thermodynamic limit. According to Eq. (3) and the condition $\Delta_{\text{T}}\tau > \hbar/2$, this phase boundary depends on the density and, within the lowest sub-band, ranges from $n_{2\text{D,int}} \approx 10^{12} \text{ cm}^{-2}$ to $n_{2\text{D,int}} \approx 2 \times 10^{12} \text{ cm}^{-2}$ for a clean topological gap of $\Delta_{\text{T}} \approx 60 \mu\text{eV}$. While this estimate provides a useful target for dielectric quality, the location of the phase transition also depends on the strength of other disorder sources.

Even for average charge densities $n_{2\text{D,int}}$ larger than the above estimate, devices can have a topological phase due to mesoscopic fluctuations. As we discuss in Sec. 3.2,

a significant fraction of devices pass the TGP if the average charged impurity density is $n_{2D,int} \leq 2.4 \times 10^{12} \text{ cm}^{-2}$, and this fraction decreases as the average charged impurity density increases. This is a consequence of the rounding of the phase transition due to finite-size effects. We estimate that the bound on the peak mobility (as a function of density) for Hall bar devices fabricated on the same material stack is $\mu_{2D} > 60,000 \text{ cm}^2/\text{Vs}$ at electron densities $n_e \sim 0.6\text{-}0.8 \times 10^{12} \text{ cm}^{-2}$. The 2DEGs used in this study have peak mobility in the range $60,000\text{-}100,000 \text{ cm}^2/\text{Vs}$ in this density range. Additional details are in Appendix A.

In a similar fashion, we have optimized the design with respect to other disorder mechanisms including variations of the following parameters along the length of the wire: thickness and dielectric constant of the oxide, barrier thickness and composition, wire width, quantum well thickness, buffer composition and thickness. We have also taken into account disorder induced by imperfections in the substrate and disorder resulting from inhomogeneous superconductor growth.

3. TOPOLOGICAL GAP PROTOCOL

3.1. Overview

The goal of the TGP is to identify whether there are regions in the experimental parameter space which show signatures consistent with a topological phase. The outer sections are kept in the trivial superconducting phase by tuning their densities with the right and left plunger gates. When the wire is in the topological phase, MZMs are localized at the boundaries between the topological and trivial sections, see Fig. 2(c), and there is a non-zero bulk transport gap. In the TGP [8], the presence of MZMs and a bulk transport gap is detected by measuring the differential conductances

$$\begin{pmatrix} G_{LL} & G_{LR} \\ G_{RL} & G_{RR} \end{pmatrix} = \begin{pmatrix} dI_L/dV_L & dI_L/dV_R \\ dI_R/dV_L & dI_R/dV_R \end{pmatrix} \quad (4)$$

as a function of V_p and B as well as the voltages V_{TC}, V_{IC} controlling the tunnel junction transparencies, and the bias voltages $V_b = V_R, V_L$, which can be increased in order to tunnel current into states of higher energies. The currents and voltages I_R, I_L, V_R, V_L are illustrated in Fig. 4. We use the $B = 0$ local conductances at an above-gap bias voltage of $500 \mu\text{V}$ as a measure of the junction transparencies.

In the tunneling regime in which the above-gap conductance is less than e^2/h , the current paths contributing to G_{RR}, G_{LL} are illustrated in Fig. 4(a). In this regime, G_{RR} and G_{LL} directly measure the local density of states in the wire at the boundaries between the middle and, respectively, the right and left sections. Hence, ZBPs in G_{RR} and G_{LL} in the tunneling regime indicate the presence of zero-energy states in the wire with sufficient tunneling matrix elements to the leads, consistent with

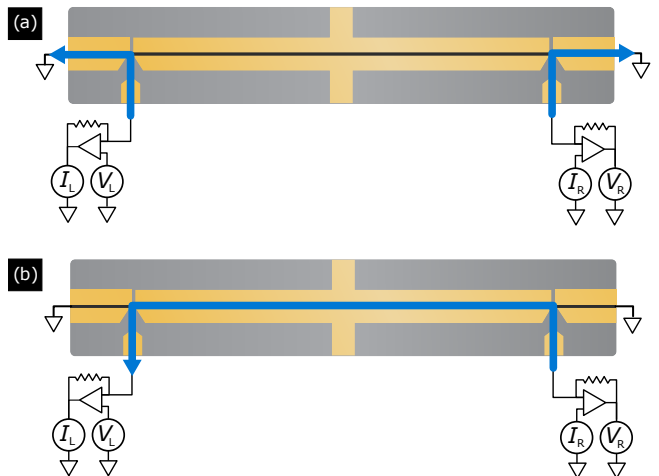


FIG. 4. Schematic illustrations of the current paths (blue arrows) that contribute to (a) G_{RR}, G_{LL} and (b) the non-local conductance G_{LR} discussed in Sec. 3.1.

MZMs but also with trivial zero-energy Andreev bound states.

The current path contributing to G_{LR} is illustrated in Fig. 4(b); G_{RL} is determined by the reverse path. For an intuitive understanding of G_{LR} and G_{RL} , we first note that in the thermodynamic limit of the wire, the clean limit, and the tunneling limit of the junctions, when the bias voltage is above the Al parent gap, an injected current will flow through the Al strip to ground via the contacts at the ends of the device unless it relaxes to energies between the induced gap and the parent gap. Hence, at bias voltages above the Al parent gap, G_{RL} and G_{LR} are strongly suppressed and are non-zero only as a result of these weak relaxation processes [78, 80, 102]. At zero-temperature, at bias voltages below the induced gap, in the thermodynamic limit of the wire, the clean limit, and the tunneling limit of the junctions, current cannot be injected into the wire, except by Andreev processes, which inject supercurrent that also flows to the grounded contacts at the ends of the device. Hence, at bias voltages below the induced gap, G_{RL} and G_{LR} are strongly suppressed and are non-zero only as a result of non-zero temperature and finite wire length. Consequently, we can determine the observed bulk transport gap from the bias voltage below which both G_{RL} and G_{LR} vanish.

There are a number of important measurement complexities that we discuss here. G_{LR} and G_{RL} may receive contributions from line impedances in the measurement circuit, which we correct for by taking the full impedance network into account [103]. In addition, we correct for finite frequency effects through calibrating resistances and capacitances in the measurement circuit. Finally, we remove any remaining voltage divider corrections and improve SNR by extracting the gap from the parts of the non-local conductances that are antisymmetric in bias voltage, $A(G_{RL}), A(G_{LR})$, per the TGP. A discussion of relevant multi-terminal conductance symmetry relations

may be found in Ref. [104].

The steps of the TGP are divided into two stages. *Stage 1:* (1) Using G_{RR} and G_{LL} , find ZBPs at each end of the wire that are stable to variations of the junction transparencies and variations in local junction potential. (2) Find clusters of points in the (B, V_{p}) plane where there are stable ZBPs at both ends of the wire. These clusters and their surrounding neighborhoods define the regions of interest ROI_1 that are the focus of Stage 2. If there are no such clusters, the device fails Stage 1.

Stage 2: (3) Focusing on smaller (B, V_{p}) ranges containing ROI_1 s and restricting to cutter gate voltage pairs for which the junction transparency is approximately the same at both ends, confirm the existence of stable zero bias peaks in G_{RR} and G_{LL} and recover the clusters of points in the (B, V_{p}) plane where there are stable ZBPs at both ends of the wire. This step is important when there is a drift in V_{p} between Stages 1 and 2. (4) Use $A(G_{\text{RL}})$ and $A(G_{\text{LR}})$ to determine the bulk energy gap as a function of (B, V_{p}) . (5) Find ZBP clusters identified in step 2 whose interiors are gapped and whose boundaries are gapless. These are the regions of interest ROI_2 . Testing this protocol against simulated data gives us high confidence that ROI_2 s have large overlap with the regions in parameter space where there is a topological phase, as we quantify below.

In principle, this protocol should detect any topological phase with a sizable gap. Finite experimental resolution and temperature, however, may obfuscate some of the topological signatures, giving rise to subtleties when interpreting the data that we discuss here.

First, a wire may have MZMs, but one or both of them may be slightly displaced from the end of the wire for some particular junction transparency controlled by the cutter gate voltages and, therefore, may not be visible. (Indeed, we see in Fig. 2(c) that the local density of states can be peaked a few hundred nanometers away from the junction.) For this reason, we do not insist that a ZBP be present for all junction transparencies and, instead, consider a ZBP to be stable in Stage 1 if it is visible for at least 70%, of junction transparencies. In Stage 2, we consider it to be stable if it is visible for the majority of junction transparencies. (In Stage 2, we only consider a restricted set of cutter gate voltage pairs in which the junction transparency is approximately the same at both ends.)

Second, the transport gap extracted from $A(G_{\text{RL}})$ will not, in general, be the same as that extracted from $A(G_{\text{LR}})$. The underlying transport gap is the same, but the transmission probability from the right junction to the left junction may not be the same as from the left to the right. [We will see an example of this in simulated data in Fig. 7(b,c) in Sec. 3.2.] This can obscure a gap narrowing or closing. Hence, for any given V_{p} and B , we determine the induced gap as the lower of the gaps extracted from $A(G_{\text{RL}})$ and $A(G_{\text{LR}})$. Consequently, the observation of non-vanishing $A(G_{\text{LR}})$ or $A(G_{\text{RL}})$ at bias voltages approaching zero is a signature of a bulk phase

transition. Note that the energy spectrum can be gapless due to the presence of disorder-induced localized states at low energies. The observed transport gap, extracted from $A(G_{\text{LR}})$ and $A(G_{\text{RL}})$, is the gap that we really care about since it is more predictive of qubit performance.

Third, $A(G_{\text{RL}})$ and $A(G_{\text{LR}})$ tend to be small at low bias voltage (due to their anti-symmetry in bias voltage) and will be suppressed even further by disorder and non-uniformity, so a gap closing may not be visible even when it is present. Another reason why an ROI_2 may be gapless along less than 100% of its boundary is that neighboring gapped regions may have been misidentified as non-topological (e.g. due to weak coupling of the MZMs to the leads or ZBP splitting due to a small topological gap). In case of such misidentification, such regions should actually be included in the ROI_2 , which would be larger and gapless along its entire boundary. To account for both of these possibilities, we only require 60% of the boundary of a cluster to be gapless as inferred from transport measurements. This 60% threshold and the previous one for stability with respect to cutter gate variation are informed by our simulations, where we observe that, at experimentally-relevant resolution, “false negative” outcomes of the TGP for true topological phases dominate for $> 60\%$ thresholds for stability of ZBPs and for the fraction of the boundary that must have visible gap closings in $A(G_{\text{RL}})$ and $A(G_{\text{LR}})$. Conversely, we do not find that allowing for a 60% threshold, rather than requiring 100%, leads to “false positives” in simulations. We do not expect a second-order phase transition to terminate (and, at least in Landau theory, a second-order phase transition cannot simply terminate, although it can turn into a first-order phase transition at a tricritical point), so if there is any arc in the phase diagram along which there is a clear gap closing/re-opening, we expect that arc to extend to a closed curve dictated by one of these two mechanisms.

Fourth, in a finite-length wire at non-zero temperature, $A(G_{\text{RL}})$ and $A(G_{\text{LR}})$ will never truly vanish at zero bias because there will at least be tunneling $e^{-L/\xi}$ and thermally-activated $e^{-\Delta/T}$ contributions.³ Hence, we need to give an operational definition for $A(G_{\text{RL}}) \approx 0$ and $A(G_{\text{LR}}) \approx 0$. We define a threshold value G_{th} which is equal to 0.05 times the maximal value of the non-local conductance at bias voltages greater than the induced gap (scanning over all B for each V_{p}). Then, if $A[G_{\text{LR}}(V_{\text{R}})], A[G_{\text{RL}}(V_{\text{L}})] < G_{\text{th}}$, we interpret this as $A[G_{\text{LR}}(V_{\text{R}})], A[G_{\text{RL}}(V_{\text{L}})] \sim O(e^{-L/\xi}, e^{-\Delta/T})$. The extracted gap is the highest bias voltage V_{b} below which $A[G_{\text{LR}}(V_{\text{b}})] < G_{\text{th}}$ and $A[G_{\text{RL}}(V_{\text{b}})] < G_{\text{th}}$. Our choice of G_{th} is not fundamental, but is purely practical. In our simulations, we find that taking G_{th} to be 0.05 times the high bias conductance does not introduce any false positives. If we take a lower value, such as 0.03 times the high

³ See also, Ref. 105 for additional considerations that are relevant to the non-local conductance.

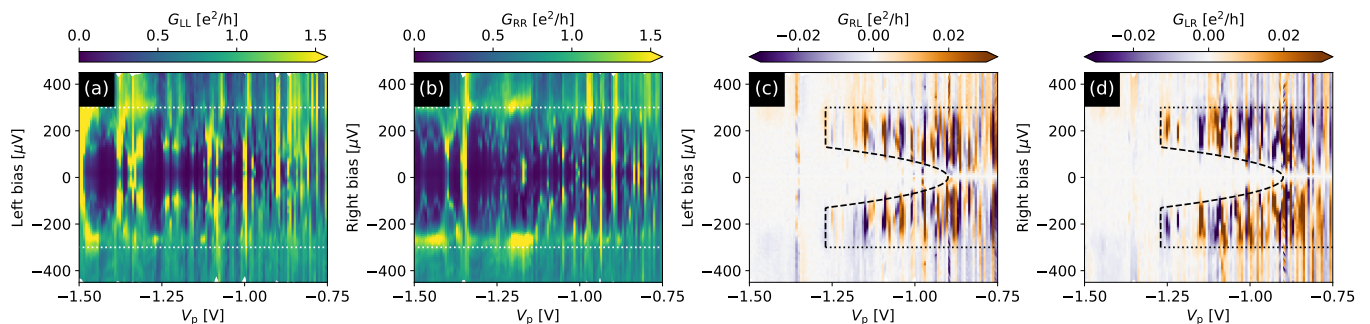


FIG. 5. The experimental local and anti-symmetrized non-local conductances for device A at zero magnetic field as a function of plunger gate voltage V_p and bias voltage. The anti-symmetrized non-local conductances in panels (c) and (d) are suppressed above the parent Al gap, which is indicated by horizontal dotted lines. They are non-vanishing down to small bias for V_p more positive than ≈ -0.9 V, which indicates that there is conduction through the region of the 2DEG that is not underneath the Al strip. This region of the 2DEG is depleted for V_p more negative than approximately -0.9 V. The anti-symmetrized non-local conductances vanish for plunger gate voltages below $V_p \approx -1.27$ V, which we identify as the bottom of the lowest sub-band. For $-0.9 \text{ V} \lesssim V_p \lesssim -1.27 \text{ V}$, the induced gap is indicated by a dashed curve which terminates in dashed vertical lines at the depletion voltage. The parent gap is visible in the local conductances in panels (a) and (b), but it is more challenging to identify the induced gap due to sub-gap states in the junctions.

bias conductance, then we will obtain a smaller topological region and a lower topological gap but a clearer gap closing. On the other hand, if we increase the threshold too much, then we will introduce false positives. Moreover, this definition of G_{th} can be applied equally well to simulated data as to measured data (unlike, for instance, a G_{th} that depends on a particular measurement setup). When we plot either simulated or measured $A[G_{\text{LR}}(V)]$, $A[G_{\text{RL}}(V)]$, we will use a black curve to indicate the bias voltage (as a function of B field) below which each one is less than G_{th} , see, e.g., Fig. 7(e,f). We can restate the threshold defined in this paragraph as follows: there is a truly sharp distinction between the trivial and topological phases only in the infinite-size, zero-temperature, and infinitesimal transparency limits; hence the threshold gives a simulation-tested method for finding the rounded transition.

A fifth subtlety is that $A[G_{\text{LR}}(V_R)]$, $A[G_{\text{RL}}(V_L)]$ can be either positive or negative, depending on whether transport at that bias voltage is primarily due to electrons or holes. It can change sign as the matrix elements change as a function of B or V_p , passing through zero when this occurs [102]. Such a sign change can appear as a very sharp increase in the induced gap, centered about some B or V_p value. In determining the zero-field induced gap, we simply avoid these points. The situation is slightly more complicated for the topological gap, since it varies between zero at the phase transition and a maximum value, which determines the stability of the topological phase. Hence, we will report both the median value of the gap over the ROI_2 and also its maximum value. However, we will not extract the maximum from the single point at which it is largest. It is not uncommon to have a very small region over which the extracted topological gap is very large because one of the aforementioned sign changes occurs, suppressing the signal in G_{LR} and G_{RL} . Hence, we define the “maximum topological gap” $\Delta_{\text{topo}}^{\text{max}}$

to be the upper quintile of measured gap values within ROI_2 .

Finally, we note that the extracted transport gap and, therefore, the phase diagram depend on the junction transparencies (and, thereby, on the cutter gate voltages that control them). A device only passes the protocol if there is an ROI_2 for at least two different junction transparencies. Since stability with respect to junction transparency is already implied by the definition of a stable ZBP, the preceding requirement essentially means that there must be a gap closing and re-opening in $A(G_{\text{RL}})$ and $A(G_{\text{LR}})$ along $> 60\%$ of the boundary for at least two different junction transparencies. This requirement is sufficient to eliminate false positives when analyzing simulated data.

The high-dimensional nature of the parameter space that is explored by the TGP makes it prudent to narrow the measured parameter range. The range of junction transparencies is determined by limiting the high-bias local conductance to the range $0.3\text{-}0.9 e^2/h$ as a compromise between sufficient visibility and remaining in the tunneling regime.

Meanwhile, the parameter range of V_p is chosen to be close to the bottom of the first sub-band. When the chemical potential is below the first sub-band, the wire is depleted. The depletion point is identified by scanning the non-local conductance as a function of bias and V_p . This can be done at $B = 0$ or at non-zero B , with B below the critical field of the superconductor, where the signal is generally larger. Recall that, as noted above, the non-local conductances are essentially zero outside the range of bias voltages between the induced and parent gaps, except for finite-size effects, thermal activation, and relaxation effects. Hence, full depletion of the wire causes the non-local conductance at bias voltages below the Al gap to drop below the noise floor. We use this depletion point to identify the single-sub-band regime.

In Fig. 5, we show the the four elements of the conductance matrix as a function of bias voltage V_b and plunger gate voltage V_p at zero magnetic field in device A to illustrate how the depletion point is identified. As may be seen from Fig. 5(c,d), the anti-symmetrized non-local conductances are small above the parent Al gap of $\Delta_{Al} = 295 \pm 8 \mu\text{eV}$, which is indicated by horizontal dotted lines in Fig. 5(c,d). The anti-symmetrized non-local conductances are non-vanishing down to small bias, which indicates that there is conduction through the 2DEG for for V_p more positive than $\approx -0.9\text{V}$. For V_p more negative than $\approx -0.9\text{V}$, the 2DEG is depleted, and the induced gap opens up, as indicated by the dashed curves. As discussed previously, the anti-symmetrized non-local conductances are large between the induced and parent gaps, are suppressed above the parent Al gap, and are very strongly suppressed below the induced gap. As V_p is decreased further, the induced gap increases, eventually reaching its maximum value of $\Delta_{ind} = 129 \pm 12 \mu\text{eV}$. At $V_p \approx -1.25\text{V}$, the anti-symmetrized non-local signal drops sharply while local conductances remain large. For more negative V_p , the anti-symmetrized non-local signal is very small, and there is no longer a visible bias range between the induced and parent gaps. This is interpreted as full depletion of the semiconductor below the Al strip. The single-sub-band regime occurs just before wire depletion.

3.2. Topological Gap Protocol applied to simulated data

We now subject simulated data to the TGP. We have generated 38 disorder realizations with the average charged defect density and non-uniformity expected for our devices and calculated these devices' differential conductances (4). (There were 50 simulated disorder realizations in total, but the junctions did not pinch off in 12 of them.) We have used this data to test the TGP and evaluate its reliability. The inferred topological phase diagram - the output of the TGP — can be compared with a topological indicator (the “scattering invariant” [106]) to estimate the probabilities of false positives and to calibrate the TGP. Additionally, these simulations have enabled us to study realization-to-realization variations in our devices and to estimate the yield of devices passing the TGP as well as to extract the maximum topological gap.

For the sake of concreteness, we now focus on one particular disorder realization in a narrow $3 \mu\text{m}$ long device with the geometry described in Sec. 2; we will call this simulated disorder realization 1, denoted R1 for short. We have computed transport through this device at $T = 30\text{mK}$, which we now discuss. In Appendix B, we discuss simulated data from two other realizations that we call realizations 2 and 3.

Stage 1: Stage 1 focuses on ZBPs in the local conductance. From the local conductances G_{RR} and G_{LL} , we can

map out the regions in (B, V_p) space where there are stable ZBPs at the two junctions, where “stable” means that the ZBPs are present for a cutter gate fraction $> 70\%$. Here, “cutter gate fraction” is the fraction of junction transparencies (or, equivalently, cutter gate settings) for which a ZBP is present. For instance, suppose we pick 5 cutter gate voltages V_{rc} at the right junction such that the above-gap conductances at the right junction are $0.25, 0.5, 0.75, 1, 1.25e^2/h$ and similarly pick 5 cutter gate voltages V_{lc} at the left junction so that the above-gap conductances at the left junction range over the same 5 values. Then, a (B, V_p) -point will be said to exhibit stable ZBPs at both junctions if there are ZBPs at both junctions for $> 17/25$ cutter gate pairs (V_{rc}, V_{lc}) . For simulated disorder realization 1, stable ZBPs at the left junction are shown in Fig. 6(a) and at the right junction are shown in Fig. 6(b). A topological phase should have stable ZBPs at both junctions at the same B, V_p , so Fig. 6(c) shows the phase space locations where there are stable ZBPs at both junctions. This is the output of Stage 1 of the TGP.

Stage 2: In the simulated data, there is no drift of the plunger gate voltage, so the ROI_1 is automatically recovered. However, we do obtain the dependence of G_{RR} and G_{LL} on the bias voltage, as seen in Fig. 7(c) and d. The more significant new ingredient in Stage 2 is the bias-dependence of the non-local conductances G_{RL} and G_{LR} , from which we determine the transport gap as a function of (B, V_p) . For simulated disorder realization 1, the non-local conductances G_{RL}, G_{LR} and the derived gap (indicated by black curves) as a function of B for $V_p = -1.37275\text{V}$ are shown in Fig. 7(e,f). Note that this cut passes through the topological phase transition and the topological phase; a clear gap closing and re-opening is seen in G_{RL} and G_{LR} . Combining the local and non-local information, we can classify any point in phase space as gapped without stable ZBPs, gapped with stable ZBPs, gapless without stable ZBPs, or gapless with stable ZBPs. These are depicted in Fig. 7(a) as, respectively, blue, orange, white, or yellow. If an orange region is surrounded by white or yellow along more than 60% of its boundary, we identify it as an ROI_2 and give it a black boundary in Fig. 7(a).

As we can see in Fig. 7(a,b), the TGP finds a region of topological phase (shown in orange in panel (a) and red in panel (b)) around $B = 1.5\text{T}$, $V_p = -1.373\text{V}$ with a maximum topological gap $\Delta_{\text{topo}}^{\text{max}} = 30 \mu\text{eV}$, which is the upper quintile of the gaps extracted in ROI_2 . The topological gap increases from zero at the phase transition to $\Delta_{\text{topo}}^{\text{max}}$ in such a way that its median value over the region within the black line in Fig. 7(a,b) is $25 \mu\text{eV}$. The TGP phase diagram is compared with a topological indicator SI (the “scattering invariant” [106]) which is also derived from the scattering matrix used to calculate the conductance tensor. The topological indicator can be defined at either junction as $\text{SI}_\alpha = \det r_\alpha \in [-1, 1]$, where r_α is the reflection matrix and $\alpha = \text{L, R}$. In Fig. 7(a), the region with negative scattering invariant on the left $\text{SI}_L < 0$

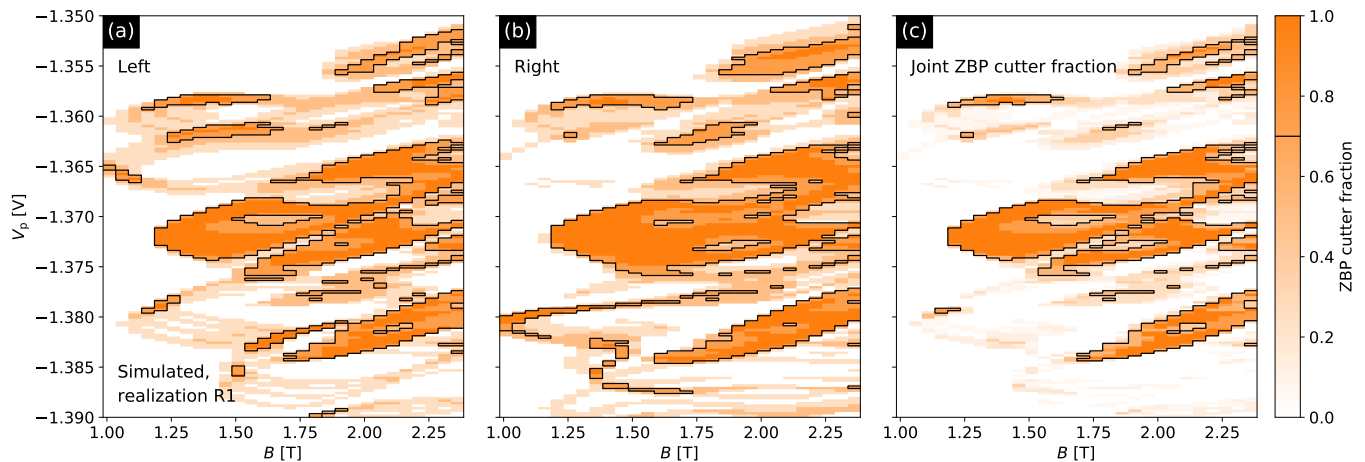


FIG. 6. The TGP applied to simulated transport data for a narrow $3\ \mu\text{m}$ long wire with $n_{2\text{D},\text{int}} = 2.4 \times 10^{12}\text{cm}^{-2}$, highlighting regions of phase space with stable ZBPs in (a) G_{LL} and (b) G_{RR} . (c) Regions of phase space with stable ZBPs in both G_{LL} and G_{RR} . Simulated transport data such as this are used to test the TGP. Here, we show one particular disorder realization for illustrative purposes. Any possible visible resemblance to measured data is dependent on the disorder realization and does *not* play a role in our analysis.

or on the right $\text{SI}_{\text{R}} < 0$ is hatched. As may be seen in Fig. 7(a), the region identified by the TGP lies almost entirely within the region with negative topological indicator, i.e. the TGP is fairly conservative and identifies a subset of the topological phase. It is not a perfect match, of course, since the TGP is not directly calculating the scattering invariant and, moreover, the phase transition is rounded by finite temperature and finite size corrections.

Fig. 7(b) is another version of the phase diagram for this disorder realization: it shows the transport gap extracted from G_{RL} and G_{LR} multiplied by $Q = \pm 1$, depending on whether that point lies outside or inside the ROI_2 . The color scale of Fig. 7(b) can be viewed intuitively as the magnitude of the bulk gap multiplied by a proxy for the sign of the topological invariant. Darker red corresponds to larger topological gap.

As expected, there are some points along the boundary of the ROI_2 where the closing is not visible in either G_{RL} or G_{LR} . 78% of the boundary of the ROI_2 region identified as topological shows a gap closing in G_{RL} , G_{LR} for this particular disorder realization. One possible reason for not finding a fully gapless boundary is that the localization length may be too short or the matrix elements too small at those parameter values, suppressing the low-bias signal in G_{RL} and G_{LR} . In such a case, the gap also closes along the remaining 22% of the boundary, but the closing is simply not visible in G_{RL} or G_{LR} . An alternative explanation is that the gapped section of the boundary of the ROI_2 is not, in fact, the boundary of the topological region but is, instead, within it. In this scenario, the boundary of the topological region is farther out, and the region between the ROI_2 and the actual boundary of the topological phase supports MZMs that have low visibility in G_{RR} and G_{LL} or are split due to hybridization facilitated by a small gap, thereby leading

to its misidentification as trivial. A comparison between the orange region in Fig. 7(a) and the hatched region testifies to the plausibility of the latter explanation: the blue region below and to the right of the orange region is hatched, indicating that it has been misclassified as a non-topological. However, as may be seen in Fig. 7(b), the ostensibly gapped region below and to the right of the ROI_2 is light blue, indicating that it has a small gap. Hence, if it were topological, it would have a small topological gap and would not be useful for a topological qubit, in contrast to the darkest red regions within the ROI_2 .

Having discussed the simulation of a single disorder realization of the device design of Fig. 2, we now consider the statistics of such disorder realizations. We have performed $T = 0$ simulations of 38 different disorder realizations in a narrow device with a $3\ \mu\text{m}$ long central section and $n_{2\text{D},\text{int}} = 2.4 \times 10^{12}\text{cm}^{-2}$. Nine of the realizations failed Stage 1. Nineteen of the realizations passed Stage 1 but failed Stage 2. Ten of the realizations passed both Stages of the TGP. In Appendix B, we show data from one realization that failed Stage 1 and one that passed Stage 1 but failed Stage 2. Every ROI_2 in a realization that passed both Stages had scattering invariant -1 indicating topological order over most of its area (83%, on average). In the 10 passing realizations, there is a significant realization-to-realization variation in the precise shape of the topological phase diagram and the size of the topological gap, as expected in a mesoscopic system.

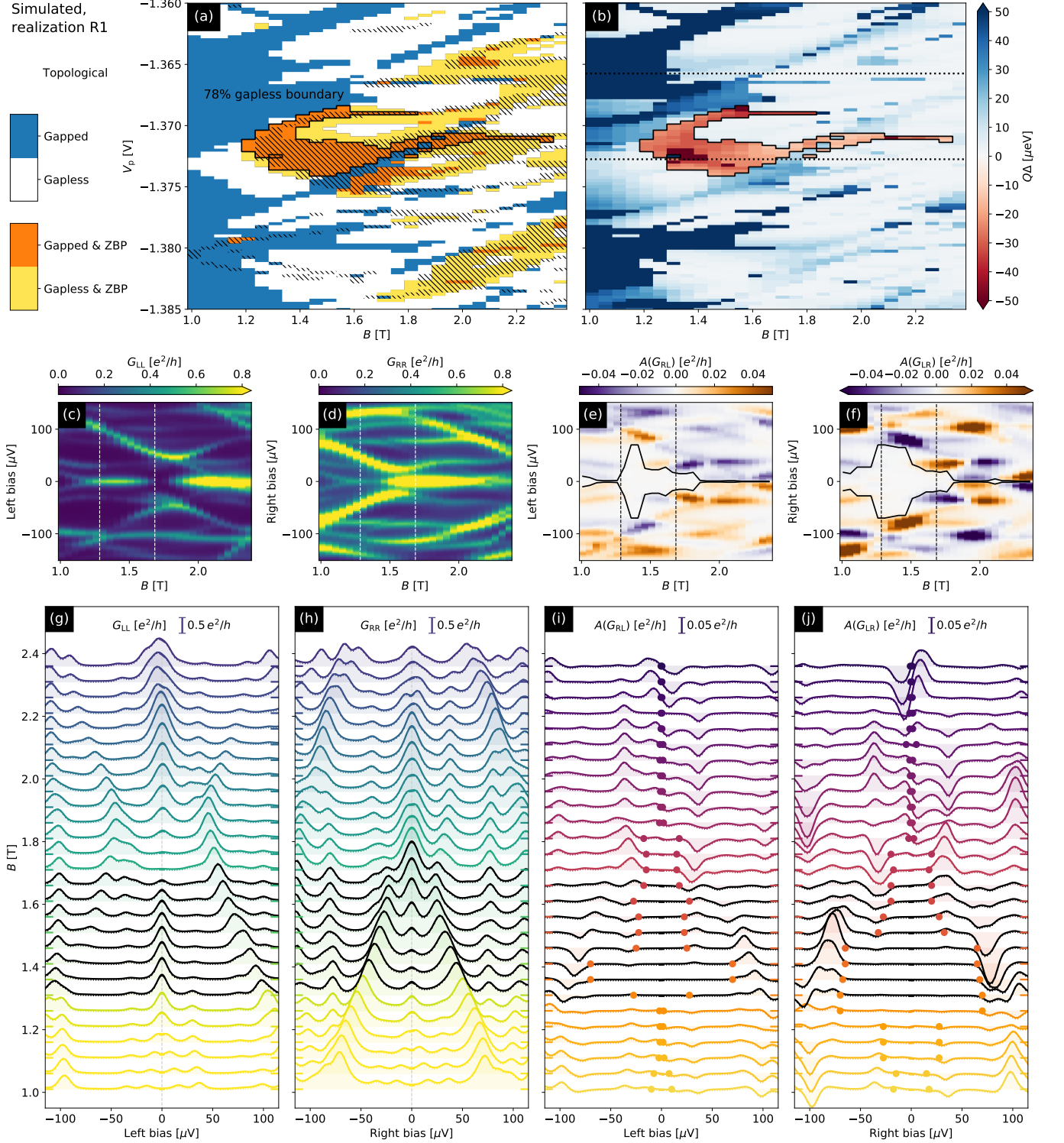


FIG. 7. (a) The simulated phase diagram for disorder realization 1 for a narrow 3 μm long wire with $n_{2D,\text{int}} = 2.4 \times 10^{12} \text{cm}^{-2}$ at $T = 30 \text{mK}$, combining the clusters of stable ZBPs at both junctions with the map of zero/non-zero gap. We identify gapped/gapless regions, with/without stable ZBPs, according to the color legend on the left. 78% of the boundary of the ROI₂ is gapless. The hatched regions are where the topological invariant is negative. (b) The simulated phase diagram, showing trivial and topological phases, as identified by the TGP. $Q = \pm 1$ in the trivial/topological phase, so the color scale shows the size of the trivial (blue) or topological (red) gap. The protocol assigns a maximum topological gap (defined as the top quintile of measured gaps within the ROI₂) of $\Delta_{\text{topo}}^{\text{max}} = 30 \mu\text{eV}$. The lower and upper horizontal dotted lines correspond to the cuts shown, respectively, in panels (c)-(f) and in Fig. 20. Simulated local and antisymmetrized non-local conductances at $V_p = -1.37275 \text{V}$: (c) G_{LL} , (d) G_{RR} , (e) $A(G_{RL})$, (f) $A(G_{LR})$. The field range between the vertical lines is in the ROI₂. Panels (g)-(j) are “waterfall” plots representing the same simulated data. The black curves in panels (e) and (f) and the dots in panels (i) and (j) are *not* guides to the eye; they indicate where the non-local signal drops below a threshold value, as described in the text. The details of these plots are disorder-dependent, and any visible resemblance to measured data does *not* play a role in our analysis.

4. EXPERIMENTAL DATA

4.1. Measurements of device A

In the remainder of this paper, we focus on measurements on devices such as the one shown in Fig. 2. In this section, we focus on data from device A (narrow Al strip and $3\ \mu\text{m}$ long wire) and discuss three experimental measurements from this device yielding the phase diagrams shown in Figs. 9, 11 and 12. Measurement A1 was taken in a different cooldown of device A and in a different dilution refrigerator than measurements A2-A3. The superconducting gap in the Al strip and the maximum induced gap at zero B -field are $295 \pm 8\ \mu\text{eV}$ and $129 \pm 12\ \mu\text{eV}$, respectively, which indicates that the induced gap to parent gap ratio (0.44) is well within the desired range. The effective charged impurity density at the interface with the dielectric is $n_{2\text{D,int}} = 2.7 \times 10^{12}\ \text{cm}^{-2}$, as is discussed in Appendix A. This value satisfies the specification explained in Sec. 2.5, which is based on the assumption that the average charged impurity density at the dielectric-semiconductor interface in the Hall bar is the same as at the dielectric-semiconductor interface in a topological gap device (the boundary between light blue and grey on either side of the Al strip in Fig. 2(d)) on the same chip. The critical field, B_c , for the thin Al strip is $> 4.5\ \text{T}$ for magnetic fields in the direction of the strip. The single sub-band regime, as determined from the non-local conductance in the same manner as in Fig. 5, is reached at a mid-plunger gate voltage between -1.2 and $-1.4\ \text{V}$ (depending on the cooldown). This is consistent with our simulations for device A; see Fig. 3. The base temperature in our measurements is $\sim 20\ \text{mK}$ and, using NIS thermometry [107], we measured an electron temperature $T_e < 40\ \text{mK}$.

4.1.1. Topological Gap Protocol Stage 1

In Stage 1 of the TGP, we do not sweep V_b . Instead, we keep $V_b = 0\ \text{V}$ on both sides while applying a lock-in excitation of $V_{\text{AC}} = 10\ \mu\text{V}$ and look for regions where $d^3 I_{\text{R}}/dV_{\text{R}}^3$ is negative and above the noise level, which indicates the presence of a peak in $dI_{\text{R}}/dV_{\text{R}}$ at zero bias, and similarly for the left junction. This is obtained from the 3ω component of the lock-in amplifier signal [108]. This enables us to scan over a large area in phase space by varying four parameters — B, V_p , and two junction transparencies (modulated via the cutter gate voltages $V_{\text{lc}}, V_{\text{rc}}$) — and by limiting the cutter gate configurations. In Stage 2, we will also sweep V_b , but will restrict (B, V_p) to smaller ranges.

We begin by finding the single-sub-band regime, following the method discussed in Sec. 3.1. The signal below the Al parent gap vanishes for $V_p < -1.18\ \text{V}$, which we interpret as the point at which the wire is fully depleted. We focus our Stage 1 scans on a V_p range of $30\ \text{mV}$ above this value.

In Fig. 8(a), we show the fraction of junction transparencies (or, equivalently, cutter gate settings) at which $d^3 I_{\text{L}}/dV_{\text{L}}^3 < 0$ at $V_{\text{L}} = 0$ as a function of B and V_p . We call this the “cutter gate fraction for ZBPs at the left junction”. The black line in Fig. 8(a) encloses the region in which the cutter gate fraction for ZBPs at the left junction is greater than $> 70\%$. Similarly, in Fig. 8(b), we show the fraction of junction transparencies at which $d^3 I_{\text{R}}/dV_{\text{R}}^3 < 0$ at $V_{\text{R}} = 0$ as a function of B and V_p with the same interpretation and the analogous black line. Finally, in Fig. 8(c), we show the fraction of junction transparencies at which both $d^3 I_{\text{L}}/dV_{\text{L}}^3 < 0$ at $V_{\text{L}} = 0$ and $d^3 I_{\text{R}}/dV_{\text{R}}^3 < 0$ at $V_{\text{R}} = 0$ as a function of B and V_p ; the black line indicates the part of the phase diagram where the cutter gate fraction for ZBPs at both junctions is $> 70\%$. Stage 1 data was taken for 5 different cutter gate voltages at each junction, or in total 25 $V_{\text{lc}}, V_{\text{rc}}$ settings. The cutter gate voltages were chosen so that the above-gap conductance of each junction is in the range $0.3\text{-}0.9e^2/h$. The goal of Stage 1 is to find (B, V_p) values at which there are ZBPs at both junctions for more than 17 out of 25 $(V_{\text{lc}}, V_{\text{rc}})$ pairs or, in other words, for which the cutter gate fraction for ZBPs at both junctions is $> 70\%$. Clusters of such points are the candidate regions of topological phase yielded by Stage 1 of the TGP, dubbed ROI_1 in Ref. 8.

There are several key features in Fig. 8 worth emphasizing. First, we expect that the topological phase in proximitized nanowires should have a lobe-like shape $|g^*|_{\mu_{\text{B}}} B/2 > \sqrt{\mu^2 + \Delta_{\text{ind}}^2}$ in the absence of disorder. As a result of disorder, we expect the lobe to be “fractured,” as shown in the simulations in Fig. 6. The field of view in Fig. 8 is a single lobe corresponding to the single sub-band regime. There is additional structure visible in the phase space locations of stable ZBPs at the left and right junctions and, especially, in ROI_1 . This is the fracturing of the lobe. We have observed very similar ROI_1 s in several devices (such as devices B, C, and D). In more disordered devices (such as device E, which is discussed in Sec. 4.2), ZBPs are scattered throughout phase space, and there is no structure, which suggests a non-topological phase of matter.

The data is reproducible between successive measurement runs on the same device, as we show in Sec. 4.1.3. The system is very stable, provided that V_p is varied by $30\ \text{mV}$ or less. If the voltage is varied by more than $100\ \text{mV}$, features shift in V_p but we can recover the same ROI_1 . If a device idles for approximately a week near an ROI_1 , we find that voltages drift by at most a few mV .

We emphasize that the main goal of Stage 1 is to identify promising regions in parameter space for measurements of both the local and non-local conductances over a range of bias voltages, which are the focus of Stage 2.

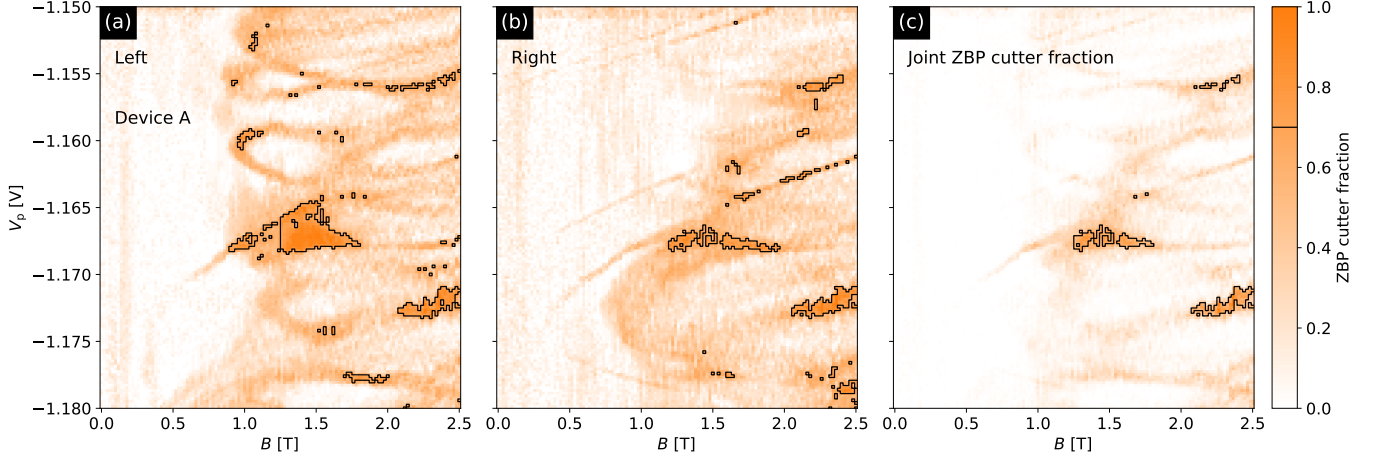


FIG. 8. Experimental ZBPs for device A, measurement A1, Stage 1 identifying ROI₁ for Fig. 9. (a) The cutter gate fraction for which there is a ZBP at the left junction as a function of B and V_p . (The color scale is at the far right.) (b) The cutter gate fraction for ZBPs at the right junction as a function of B and V_p . (c) The cutter gate fraction for ZBPs at both junctions. In all three panels, regions for which the cutter gate fraction for ZBPs is at least 70% are surrounded by black lines. The cutter gate fractions for ZBP are defined in the third paragraph of Sec. 4.1.1. ZBPs that occur at only one junction or for a small cutter gate fraction are likely to be due to trivial Andreev bound states.

4.1.2. Topological Gap Protocol Stage 2: Measurement A1

In Stage 2, we focus on the regions of the (B, V_p) plane where there are clusters of points with stable ZBPs at both junctions. We now take full voltage bias scans of the local conductances, such as Fig. 9(c,d), as well as full bias scans of the non-local conductances, such as Fig. 9(e,f). Hence, the local and non-local conductances are measured as functions of B , V_p , V_{1c} , V_{1r} , V_b . Since we are now exploring a higher-dimensional parameter space, we restrict the V_p sweep to the vicinity of ROI₁ identified in Stage 1, which is typically $\delta V_p \approx 5$ -15 mV. We further restrict the parameter space by taking scans for 3-5 cutter gate pairs (rather than the 25 pairs of Stage 1). In the measurement of device A displayed in Fig. 9, there were 3 cutter gate pairs (V_{1c} , V_{1r}). These cutter gate settings correspond to above-gap conductances (measured at 500 μ V voltage bias) of 0.3 , 0.5 , and $0.7e^2/h$ at both junctions. In Fig. 9, we show data for the representative cutter gate setting for which both above-gap junction conductances are $0.3e^2/h$ and the discussion below focuses on this data, but similar observations hold for the other two settings.

Since there is typically a small voltage drift between Stages 1 and 2, we start the analysis of the Stage 2 data by determining the regions with stable zero bias peaks anew. We call the ZBPs stable if they are present for at least 2 out of 3 cutter gate settings. In Fig. 9(c,d), we illustrate ZBPs for our representative cutter gate setting by showing G_{LL} and G_{RR} for $V_p = -1.17175$ V. In Fig. 9(b), we see that the corresponding horizontal line passes through a region with stable ZBPs.

We then use the bias scans of the non-local conductances $A(G_{RL})$, $A(G_{LR})$ to determine the bulk transport gap at each point in the phase diagram. In Fig. 9(e,f), we show $A(G_{RL})$ and $A(G_{LR})$ as a function of B at the

$V_p = -1.17175$ V horizontal line in Fig. 9(a,b). (Waterfall plots of the conductances along the $B = 1.66$ T vertical line are shown in Fig. 10.) The black curves in Fig. 9(e,f) show the transport gap extracted from, respectively, G_{RL} or G_{LR} as a function of B for this V_p value. There is a clear bulk transport gap closing and re-opening visible in $A(G_{LR})$ at $B \approx 1.5$ T. The gap remains open from $B \approx 1.5$ T to $B \approx 2.5$ T. Here, we show transport data for our representative cutter gate setting, but the ROI₂ is present for all junction settings. The transport gap is obtained by taking the minimum of the values extracted from $A(G_{RL})$ and $A(G_{LR})$. In Fig. 10, we also show “waterfall” plots of local and non-local conductances as a function of V_p at fixed $B = 1.66$ T. One can clearly see a gap closing and re-opening along the vertical line in Fig. 9(b). Combining all this data enables us to map out the transport gap as a function of B and V_p , as shown in Fig. 9(b).

Per the TGP, we synthesize the information yielded by the local and non-local conductances in Stage 2 measurements, which are taken over the range of V_p and B values identified in Stage 1. We thereby derive the experimental phase diagrams in Fig. 9(a,b). In Fig. 9(a), a vanishing gap is shown in white or yellow, and a non-zero gap is shown in blue or orange, depending on the presence of correlated stable ZBPs on both sides. The orange region has stable ZBPs at both ends and a non-zero bulk transport gap. 62% of the boundary of this region is gapless, thus yielding ROI₂. The TGP associates an ROI₂ with the topological phase because it is characterized by stable ZBPs at both ends and is separated from the trivial low-field phase by a phase boundary where the bulk transport gap vanishes. In Fig. 9(b), we present the inferred topological phase diagram for our representative cutter gate setting. (All three cutter gate settings yield

similar phase diagrams.) The topological phase (interior of ROI₂) is shaded red, with an intensity proportional to the transport gap, while the trivial phase (complement of ROI₂) is shaded blue. We note that the stability of gap extraction with respect to cutter gate setting is not a requirement of the TGP. We also pause to stress that, in simulations of 38 different disorder realizations, we found no false positives for devices that passed the TGP for at least two different pairs of cutter gate settings (i.e. junction transparencies).

We re-emphasize that the conductances G_{RR} , G_{LL} , G_{RL} , G_{LR} are not topological invariants and are not expected to have quantized values at non-zero temperature and junction transparency. So a ZBP, no matter how stable or well-quantized, cannot prove that the system is in a topological phase. Conversely, the existence of a topological phase in a device is not disproven by a ZBP that has a small magnitude or a transport gap that does not appear to close due somewhere along the putative transition line due to suppression of G_{RL} and G_{LR} at low bias by disorder. We stress that the crucial point of the TGP is to not rely on a single feature to identify a topological phase, but instead to rely on the totality of the data to provide evidence for the observation of a topological phase. First, note that we can infer a bulk gap closing and re-opening from $A(G_{RL})$, $A(G_{LR})$, which is a signature of a second-order phase transition. It is important to distinguish such behavior in the non-local conductances $A(G_{RL})$, $A(G_{LR})$ from apparent gap closings/re-openings in the local conductances G_{RR} , G_{LL} , which could easily be the motion of a local state towards zero energy, rather than a bulk phenomenon.

Secondly, we note that this phase transition line separates the high-field gapped phase from the gapped trivial superconducting phase that is present at low fields. It does not quite surround the high-field gapped phase: 62% of the boundary shows a gap closing in $A(G_{RL})$, $A(G_{LR})$, not 100%. This surpasses the threshold of 60% required by the TGP and is similar to the percentage of the boundary of the ROI₂ that is gapless in the simulated data of Fig. 7. Consequently, we believe that the second order phase transition line that surrounds 62% of our putative topological phase is, in fact, part of an unbroken transition line surrounding the entire phase. Either the gap closing is not visible along 38% of the boundary of the ROI₂ due to a suppression of the signal by disorder/non-uniformity or the topological region is larger than the ROI₂ and includes the neighboring gapped regions (such as the blue regions above and to the right of the ROI₂ in Fig. 9(a,b), which, in this scenario, have been misidentified due to poor coupling of the MZMs to the leads or splitting of ZBPs due to a collapsing gap. Indeed, for the cutter gate setting shown in Fig. 9, there are ZBPs at both junctions up to $B = 2.5$ T. At the left junction, this ZBP is very weak, but above measurement resolution, as may be seen in Fig. 9(c,g). However, there is no visible ZBP at the left junction at the other cutter gate settings. As noted previously, our simulations of

this device design and disorder/non-uniformity level indicate that this is the typically expected visibility of the phase transition line.

The high-field gapped phase is characterized by stable ZBPs at both ends of the wire, which is consistent with the topological phase. However, the ZBPs appear before the gap re-opens for some V_p values in device A, as evidenced by the yellow region to the left of the orange region in Fig. 9. This is consistent with a scenario in which “quasi-MZMs” [46–50] are precursors to the transition into the topological phase, which is frequently seen in simulations.

The maximum topological gap is $\Delta_{\text{topo}}^{\text{max}} = 23 \mu\text{eV}$. Over the ROI₂, which has an extent of $\delta B \sim 500$ mT, $\delta V_p \sim 1.5$ mV, the extracted topological gap increases from zero to $\Delta_{\text{topo}}^{\text{max}}$ in such a way that its median value over the region within the black line in Fig. 9(a,b) is $19 \mu\text{eV}$. From the phase diagram in Fig. 9(a,b), we see that the lowest field at which the gap closes near the ROI₂ is ≈ 0.8 T, which implies an effective g -factor of at least $|g_{\text{eff}}| \approx 5.6$. (Here, we define $|g_{\text{eff}}| \equiv 2\Delta_{\text{ind}}/\mu_B B_{\text{min}}$, where B_{min} is the lowest field at which the gap closes.⁴) This value of $|g_{\text{eff}}|$ is close to the optimal value for this device design and material stack.

The induced gap (and all structure associated with its closing/re-opening) decreases rapidly when the magnetic field is rotated away from the direction of the wire, as expected. The transition to the topological phase should become more smeared as the temperature is increased, but it is difficult to study this systematically due to voltage drifts.

Comparing the experimental data in Fig. 9 to the simulated data in Fig. 7, we note both the qualitative and quantitative similarity between the phase diagrams. In both simulated and measured data, there are gap closings at similar V_p -dependent B -field values, and the extent of both the gapless regions and the ROI₂s are of similar size in the B - V_p plane. However, we emphasize again that the main role of simulated data such as that shown in Fig. 7 is to test the TGP on (simulated) devices for which we know the phase diagram.

4.1.3. Reproducibility of the data: Measurements A2 and A3

We now present experimental data from a different cooldown in which measurements A2 and A3 were performed one week apart. These measurements produced

⁴ Here we define effective g -factor as the average slope of the extracted induced gap vs B -field. This is different from the conventional definition of the spin g -factor involving dE/dB at $k = 0$. The former depends on spin-orbit coupling and orbital physics whereas the latter does not. However, in the single sub-band regime, where the lowest energy state has a momentum close to $k = 0$, both orbital B -field and spin-orbit coupling effects are small. In this case, $|g_{\text{eff}}|$ is a good proxy for $|g^*|$.

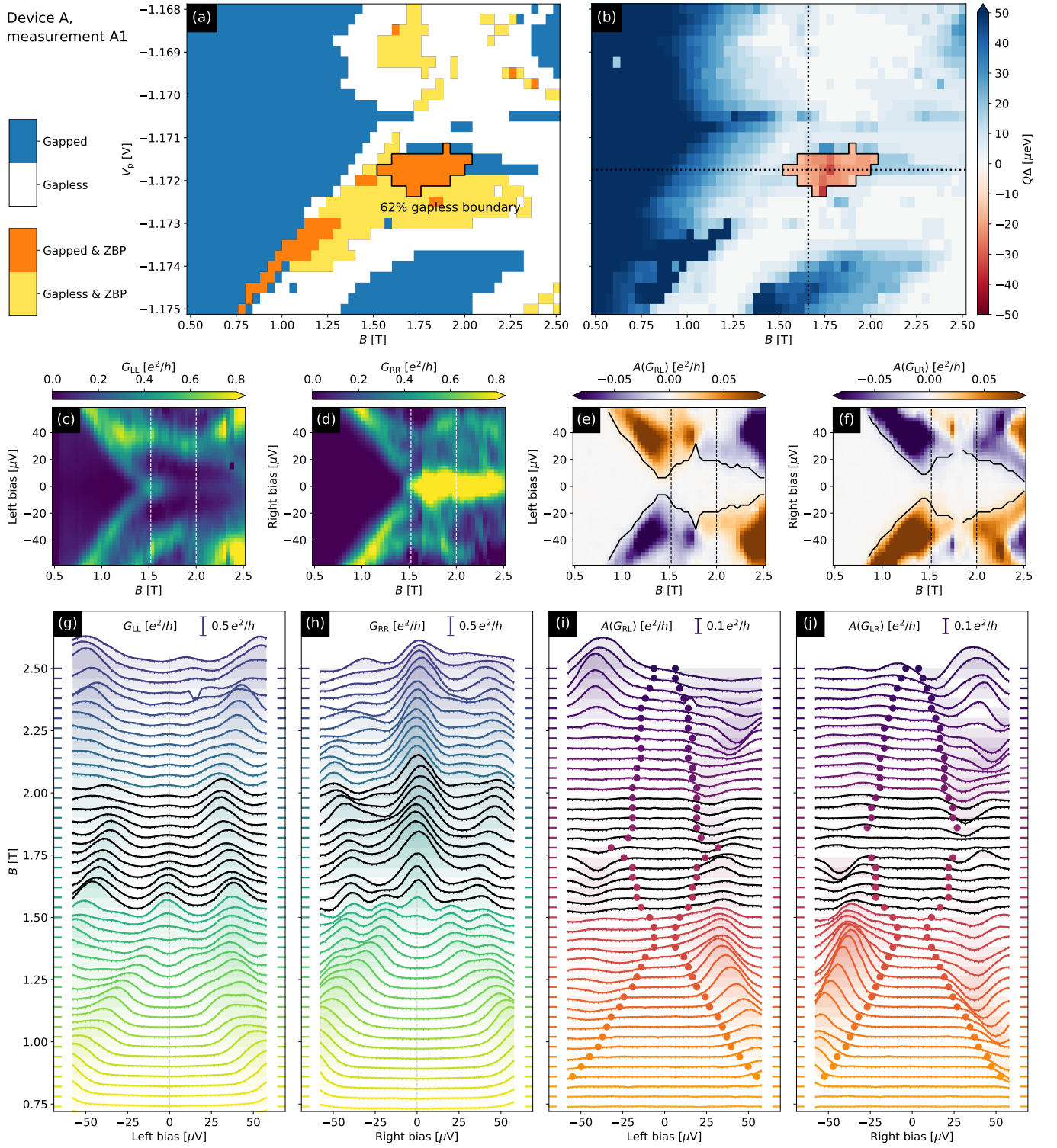


FIG. 9. (a) The experimental phase diagram of device A (measurement A1) in the color scheme shown at the left. The stability of ZBPs is determined by varying the cutter gates so that both $B = 0$ conductances take the values $0.3, 0.5, 0.7e^2/h$ at an above-gap bias voltage of $500 \mu\text{V}$. The boundary of the ROI_2 is interpreted as a phase transition line, consistent with a visible gap closure along 62% of it. (b) The experimental phase diagram, showing trival/topological phases, which the TGP identifies with the exterior/interior ($Q = \pm 1$) of the ROI_2 . The color scale shows the size of the trivial (positive sign) or topological (negative sign) gap. The protocol assigns a maximum topological gap $\Delta_{\text{topo}}^{\text{max}} = 23 \mu\text{eV}$. Measured local and antisymmetrized non-local conductances along the horizontal line in panel b at $V_p = -1.17175 \text{V}$: (c) G_{LL} , (d) G_{RR} , (e) $A(G_{RL})$, (f) $A(G_{LR})$. The ROI_2 lies between the vertical lines. Panels (g)-(j) are “waterfall” plots representing the same measured data. The data shown in (c)-(j) was obtained for above-gap left/right conductances of approximately $0.3e^2/h$. The black curves in panels (e) and (f) and the dots in panels (i) and (j) are *not* guides to the eye; they indicate where the non-local signal drops below a threshold value, as described in the text.

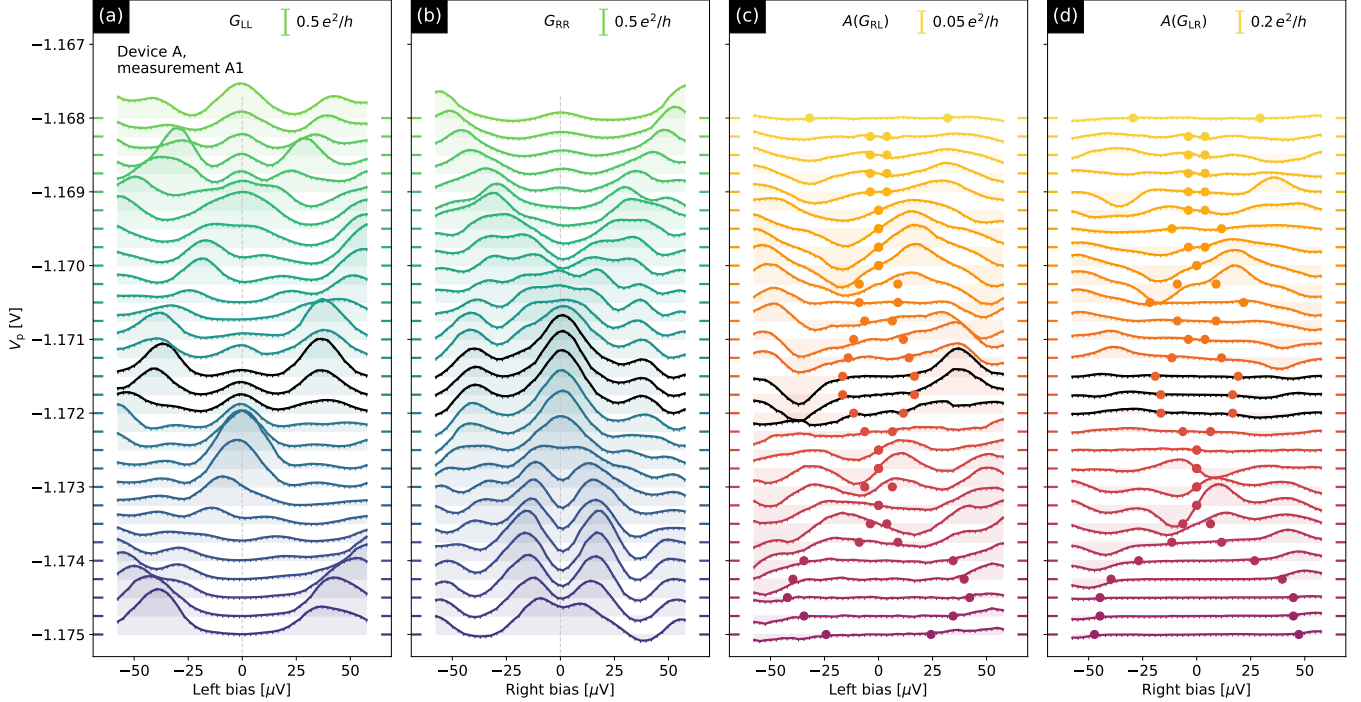


FIG. 10. “Waterfall” conductance plots of (a) G_{LL} , (b) G_{RR} , (c) $A(G_{RL})$, (d) $A(G_{LR})$ as a function of the corresponding bias and plunger gate voltage V_p for device A (measurement A1). The data is the $B = 1.66$ T vertical line in Fig. 9(b). ZBPs and extracted gap points corresponding to ROI₂ are shown in black.

similar data sets, both passing the TGP, indicating the reproducibility of our data and the device’s stability from one measurement run to another. Both of these data sets are consistent with measurement A1 shown in Sec. 4.1.

We now discuss data from re-measurement A2 of device A: device A was warmed-up, removed from the dilution refrigerator, cooled down in a different dilution refrigerator, and re-measured. Each cooldown typically leads to a somewhat different disorder configuration resulting in a shift of gate voltages at which we see, for example, the depletion of the lowest sub-band. Nevertheless, device A passed the TGP with this new disorder configuration, although the topological phase shifted in parameter space. In accordance with the TGP, we performed Stage 1 measurements and identified an ROI₁ with stable ZBPs near $V_p = -1.4$ V. The results of the subsequent Stage 2 measurement are shown in Fig. 11.

In Fig. 11(a), we see a similar lobe-like parabolic shape to that seen in measurement A1 (see Fig. 9) separating gapped states from gapless ones. The lowest gap closing point in A2 is slightly lower in field than in A1, leading to an effective g -factor of $|g_{\text{eff}}| \approx 6.4$. The topological phase starts at lower fields, close to 0.8 T, which is closer to the lowest fields at which the gap closes than in A1, and it extends over a larger range of plunger gate voltages, $\delta V_p = 2.5$ mV but a similar magnetic field range $\delta B \approx 500$ mT. The maximum topological gap in measurement A2 is $\Delta_{\text{topo}}^{\text{max}} = 29 \mu\text{eV}$, see Fig. 11(b), which is the largest observed for device A. Furthermore, the percentage of the boundary that is gapless is 82% in A2,

increased from 62% in measurement A1. The local conductances are shown in Fig. 11(c,d). In addition to ZBPs, there is also a strong local resonance at the right junction which is evident in Fig. 11(d). However, this resonance moves away from zero bias as B is increased. Furthermore, this resonance disappears in the subsequent measurement shown in Fig. 12(d), indicating that this is an accidental feature due to an impurity that moved between measurements A2 and A3. This trivial resonance partially obscures the stable ZBP which has a smaller amplitude.

In Fig. 12, we show measurement A3 which was performed approximately one week after measurement A2. As is typically the case in our devices, the electrostatic environment of the system drifted by 2-3 mV during the week between the two measurement runs. However, the main qualitative features are reproduced from one run to the next: there is a topological phase with a comparable critical field and similar overall shape. The size of the maximum topological gap has decreased from its value in A2 to $\Delta_{\text{topo}}^{\text{max}} = 22 \mu\text{eV}$, which is close to value found in measurement A1.

Finally, we discuss the stability of ZBPs with respect to local perturbations. In Fig. 12(c,d) one can see stable ZBPs at both junctions over a 0.5 T magnetic field range. This shows their stability with respect to changes in the magnetic field; they are similarly stable with respect to changes in the plunger gate voltage, as may be seen from the vertical extent of the orange/red regions in Fig. 12(a,b), respectively. These peaks are also sta-

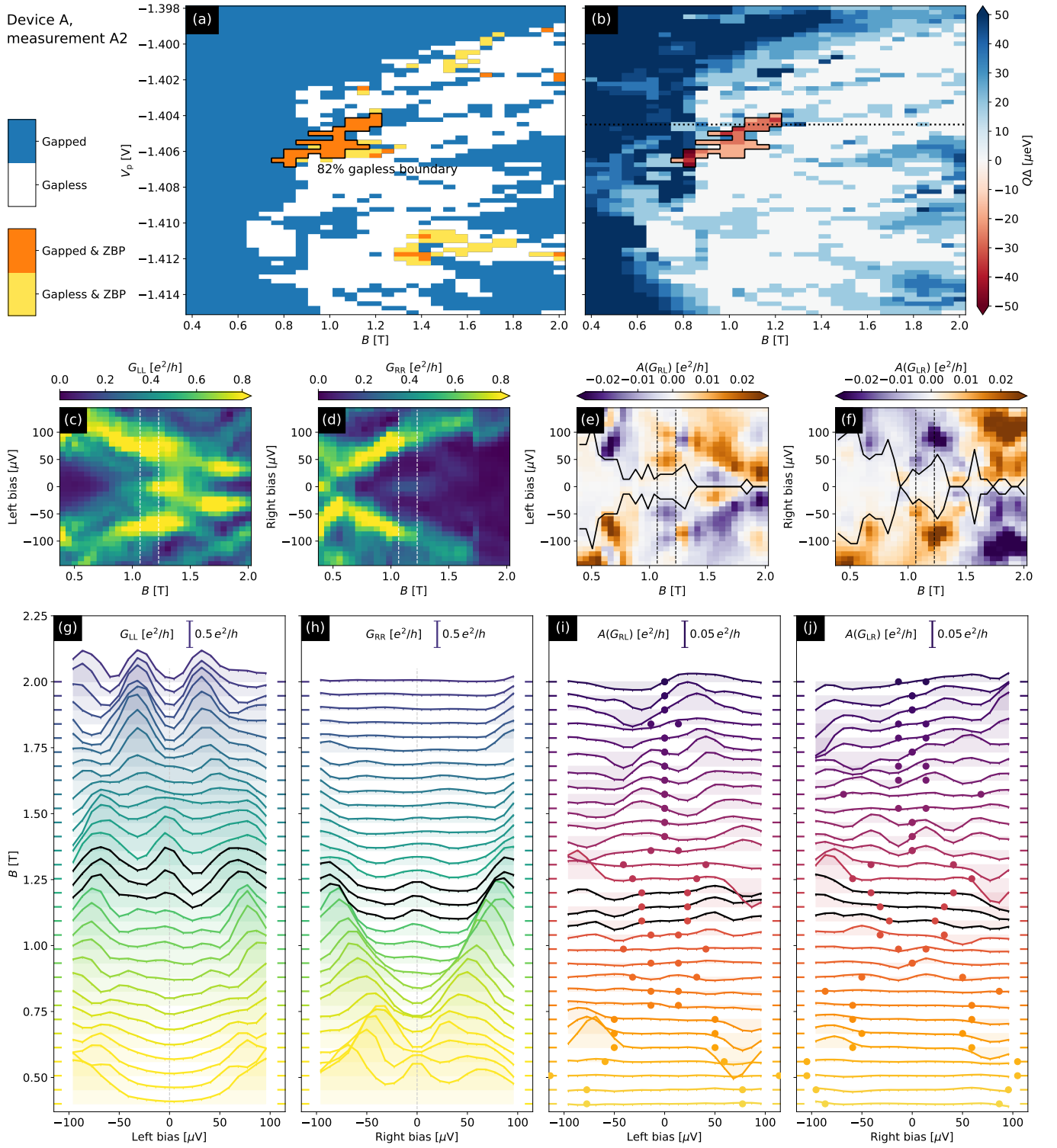


FIG. 11. (a) The experimental phase diagram of device A (measurement A2) that results from combining the clusters of stable ZBPs at both junctions with the map of the locus of zero/non-zero gap. The stability of ZBPs is determined by varying the cutter gate settings so that both $B = 0$ conductances take the values $0.3, 0.5, 0.7, 0.9e^2/h$ at an above-gap bias voltage of $500 \mu\text{V}$. The boundary of the ROI₂ is interpreted as a phase transition line, consistent with a visible gap closure along 82% of it. (b) The experimental phase diagram, showing trivial/topological phases, which the TGP identifies with the exterior/interior ($Q = \pm 1$) of the ROI₂. The color scale shows the size of the trivial (positive sign) or topological (negative sign) gap. The protocol assigns a maximum topological gap $\Delta_{\text{topo}}^{\text{max}} = 29 \mu\text{eV}$. Measured local and antisymmetrized non-local conductances along the horizontal line in panel b at $V_p = -1.4045$ V: (c) G_{LL} , (d) G_{RR} , (e) $A(G_{RL})$, (f) $A(G_{LR})$. The ROI₂ lies between the vertical lines. Panels (g)-(j) are “waterfall” plots representing the same measured data. The data shown in (c)-(j) was obtained for above-gap left (right) conductances of approximately $0.5e^2/h$ ($0.8e^2/h$). The black curves in panels (e) and (f) and the dots in panels (i) and (j) indicate where the non-local signal drops below a threshold value, as described in the text.

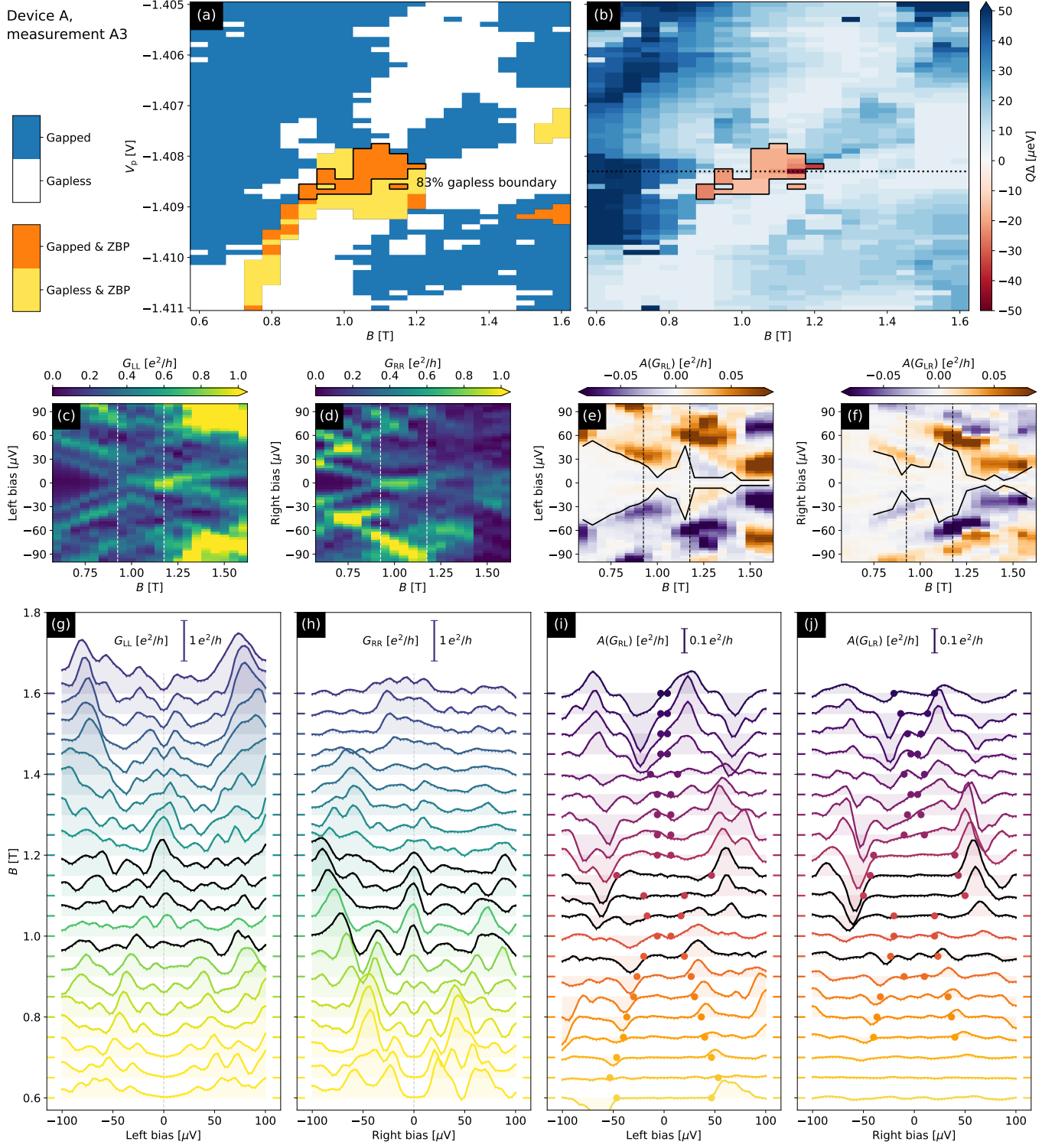


FIG. 12. (a) The experimental phase diagram of device A (measurement A3) that results from combining the clusters of stable ZBPs at both junctions with the map of the locus of zero/non-zero gap. The stability of ZBPs is determined by varying the cutter gate settings so that both conductances take four values between 0.3 and $0.8e^2/h$ at an above-gap bias voltage of $500\ \mu\text{V}$. The boundary of the ROI_2 is interpreted as a phase transition line, with a visible gap closure along 83% of it. (b) The experimental phase diagram, showing trivial/topological phases, which the TGP identifies with the exterior/interior ($Q = \pm 1$) of the ROI_2 . The color scale shows the size of the trivial (positive sign) or topological (negative sign) gap. The protocol assigns a maximum topological gap of $\Delta_{\text{topo}}^{\text{max}} = 22\ \mu\text{eV}$. Measured local and antisymmetrized non-local conductances along the horizontal line in panel b at $V_p = -1.4083\ \text{V}$: (c) G_{LL} , (d) G_{RR} , (e) $A(G_{RL})$, (f) $A(G_{LR})$. The ROI_2 lies between the vertical lines. Panels (g)-(j) are “waterfall” plots representing the same measured data. The data shown in (c)-(j) was obtained for left (right) conductances of approximately $0.6e^2/h$ ($0.4e^2/h$) at an above-gap bias voltage of $500\ \mu\text{V}$ at $B = 0$. The black curves in panels (e) and (f) and the dots in panels (i) and (j) indicate where the non-local signal drops below a threshold value, as described in the text.

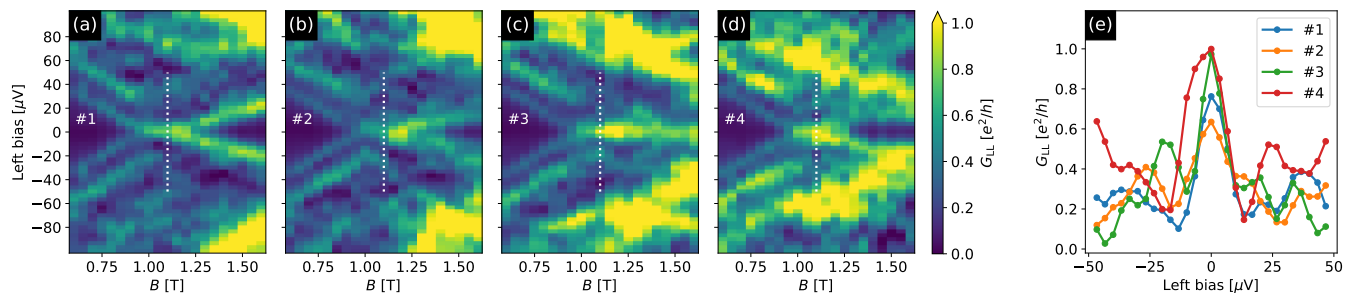


FIG. 13. (a)-(d) Bias-field cuts of measurement A3 at $V_p = -1.4083$ V. G_{LL} is shown for 4 different left cutter gate settings #1-4 corresponding, respectively, to conductances of approximately 0.5 , 0.6 , 0.7 , and $0.8e^2/h$ at an above-gap bias voltage of $500 \mu\text{V}$ at $B = 0$. Panel (b) for cutter #2 shows the same data as Fig. 12(c). (e) Line-cut at $B = 1.1$ T for the above cutter gate settings. The chosen values of B and V_p lie within ROI_2 shown in Fig. 12(b) for left and right cutters corresponding to the above-gap conductance of 0.6 and $0.4e^2/h$, accordingly. Note that the ZBP height is of the order of e^2/h for all left cutter gate settings.

ble with respect to cutter changes modulating the transparency of the junctions, as we show in Fig. 13. There are ZBPs with height $O(e^2/h)$ that are present for 4 cutter gate settings. These changes in left cutter gate settings cause the above-gap conductance to vary over the range. Thus, while these cutter changes significantly modify the junction transparencies, the ZBPs remain stable with respect to these perturbations. In ROI_2 , there are ZBPs exhibiting this type of stability at both junctions.

To conclude, we believe that the totality of the data from device A — passing the TGP in multiple cooldowns and re-measurements, qualitative and quantitative consistency with simulations, and the stability of the ROI_2 with respect to various perturbations — provides strong evidence for the observation of a stable topological superconducting phase supporting MZMs in this device. We now turn to the reproducibility of these results in other devices.

4.2. Experimental data from other devices

We now pivot to other devices in order to assess device-to-device variations. Since disorder can destroy the topological phase, and different devices will have different disorder realizations, we can expect quantitative and qualitative differences between devices. Indeed, we have measured devices that do not appear to have a topological phase. However, devices that have a narrow Al strip, zero-field induced gap to parent gap ratio in the required range, and weak disorder often pass the TGP while devices not meeting these requirements have never passed TGP, as expected from simulations. For example, no devices with dielectric charge density above $3 \times 10^{12} \text{cm}^{-2}$, as extracted from a Hall bar on the same chip, have passed TGP.

In this section, we show data from devices B and C, which also pass the TGP, thereby demonstrating that we can reproducibly fabricate devices passing the TGP. Device B has a parent Al gap and a maximum zero-field

induced gap of, respectively, $292 \pm 8 \mu\text{eV}$ and $104 \pm 6 \mu\text{eV}$; in device C, the corresponding gaps are $293 \pm 9 \mu\text{eV}$ and $117 \pm 20 \mu\text{eV}$. The ratio of the induced gap to the parent gap in devices B and C (0.35 and 0.4, respectively) is somewhat smaller than the nearly-optimal value that it takes in device A (0.43). The effective charged impurity densities at the interface with the dielectric is $n_{2\text{D,int}} = 1.1 \times 10^{12} \text{cm}^{-2}$ in device B and $n_{2\text{D,int}} = 1.0 \times 10^{12} \text{cm}^{-2}$ in device C, extracted by the procedure discussed in Appendix A. These values are smaller than in device A and satisfy the specification given in Sec. 2.5.

In addition, we show data from devices D and E that do not pass the TGP. As noted previously, we do not expect all devices to pass the TGP, even if they were to have the same gap ratio and disorder levels as device A. Hence, it is not surprising that some of our devices fail the TGP; indeed, it is required by consistency with our simulations. Moreover, devices D and E have lower induced gap to parent gap ratios, which suppresses their expected probabilities of passing the TGP. Device D has a parent Al gap and a maximum zero-field induced gap of, respectively, $415 \pm 13 \mu\text{eV}$ and $90 \pm 6 \mu\text{eV}$ (induced gap to parent gap ratio of 0.22); in device E, the corresponding gaps are $338 \pm 12 \mu\text{eV}$ and $92 \pm 14 \mu\text{eV}$ (induced gap to parent gap ratio of 0.27). The effective charged impurity densities at the interface with the dielectric is $n_{2\text{D,int}} = 3.1 \times 10^{12} \text{cm}^{-2}$ in device D and $n_{2\text{D,int}} = 3.0 \times 10^{12} \text{cm}^{-2}$ in device E, extracted by the procedure discussed in Appendix A. These values are larger than in devices A-C, and do not satisfy the specification given in Sec. 2.5.

Device D exhibits clusters of points in (B, V_p) space with stable ZBPs at both ends, thereby passing Stage 1 of the TGP. However, non-local measurements in the region of interest yield zero gap (i.e. gapless phase) and thus device D fails Stage 2 of the TGP. Device E fails even Stage 1 because it does not have clusters of (B, V_p) points with stable ZBPs at both ends.

Overall, the measurement data from devices A-E demonstrate the different qualitative phenomena ob-

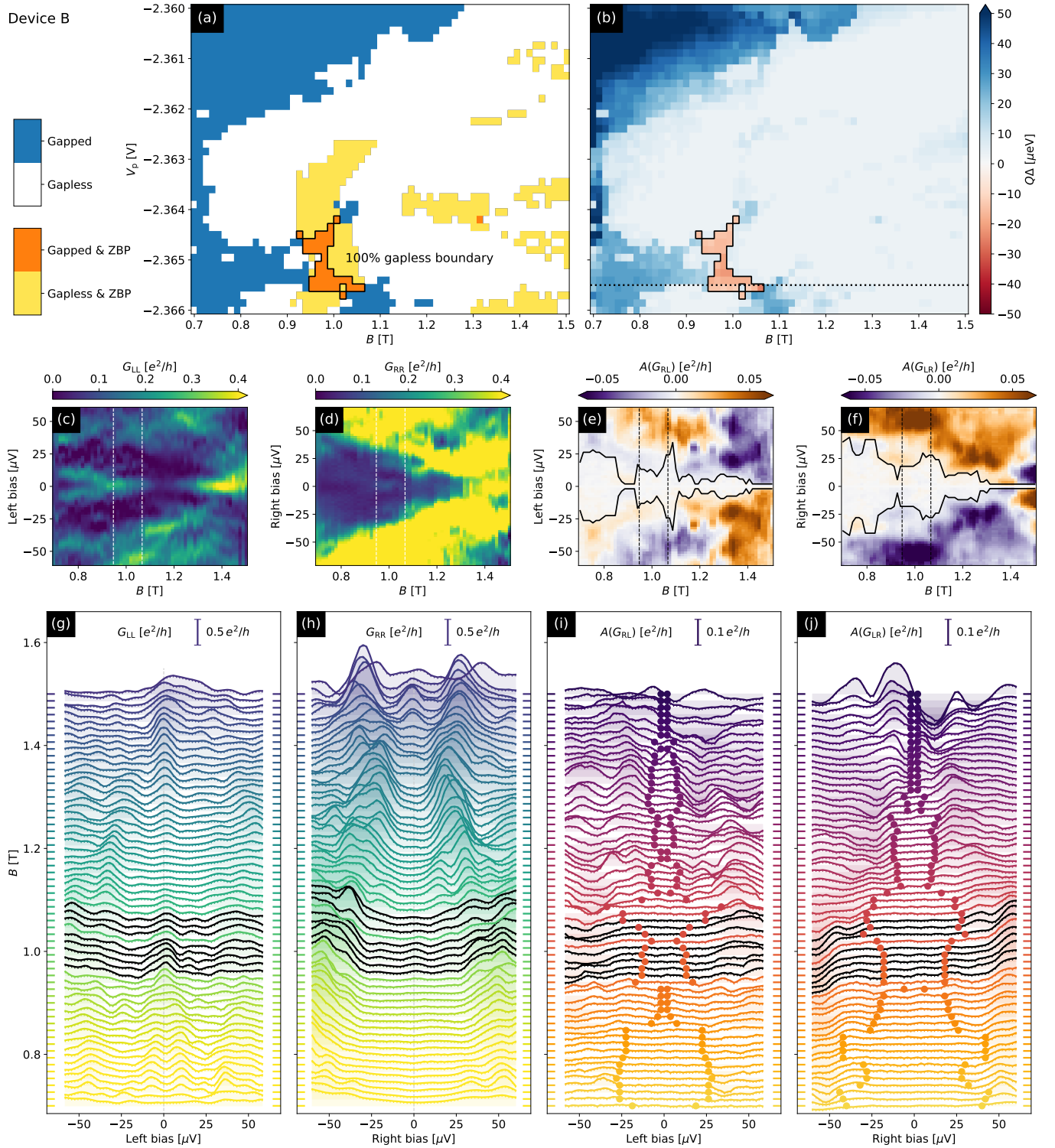


FIG. 14. (a) The experimental phase diagram of device B that results from combining the clusters of stable ZBPs at both junctions with the map of the locus of zero/non-zero gap. The stability of ZBPs is determined by varying the cutter gate settings so that the $B = 0$ conductances range from 0.6 and $1.0e^2/h$ on the left and from 0.2 and $0.4e^2/h$ on the right at an above-gap bias voltage of $500 \mu\text{V}$. The boundary of the ROI_2 is interpreted as a phase transition line, consistent with a visible gap closure along 100% of it. (b) The experimental phase diagram, showing the trivial/topological phases, which the TGP identifies with the exterior/interior ($Q = \pm 1$) of the ROI_2 . The color scale shows the size of the trivial (blue) or topological (red) gap. The protocol assigns maximum topological gap of $18 \mu\text{eV}$. Measured local and antisymmetrized non-local conductances along the horizontal line in panel b at $V_p = -2.3655 \text{ V}$: (c) G_{LL} , (d) G_{RR} , (e) $A(G_{RL})$, (f) $A(G_{LR})$. The ROI_2 lies between the vertical lines. Panels (g)-(j) are “waterfall” plots representing the same measured data. The data shown in (c)-(j) was obtained for above-gap left (right) conductances of approximately $0.6e^2/h$ ($0.2e^2/h$). The black curves in panels (e) and (f) and the dots in panels (i) and (j) indicate where the non-local signal drops below a threshold value, as described in the text.

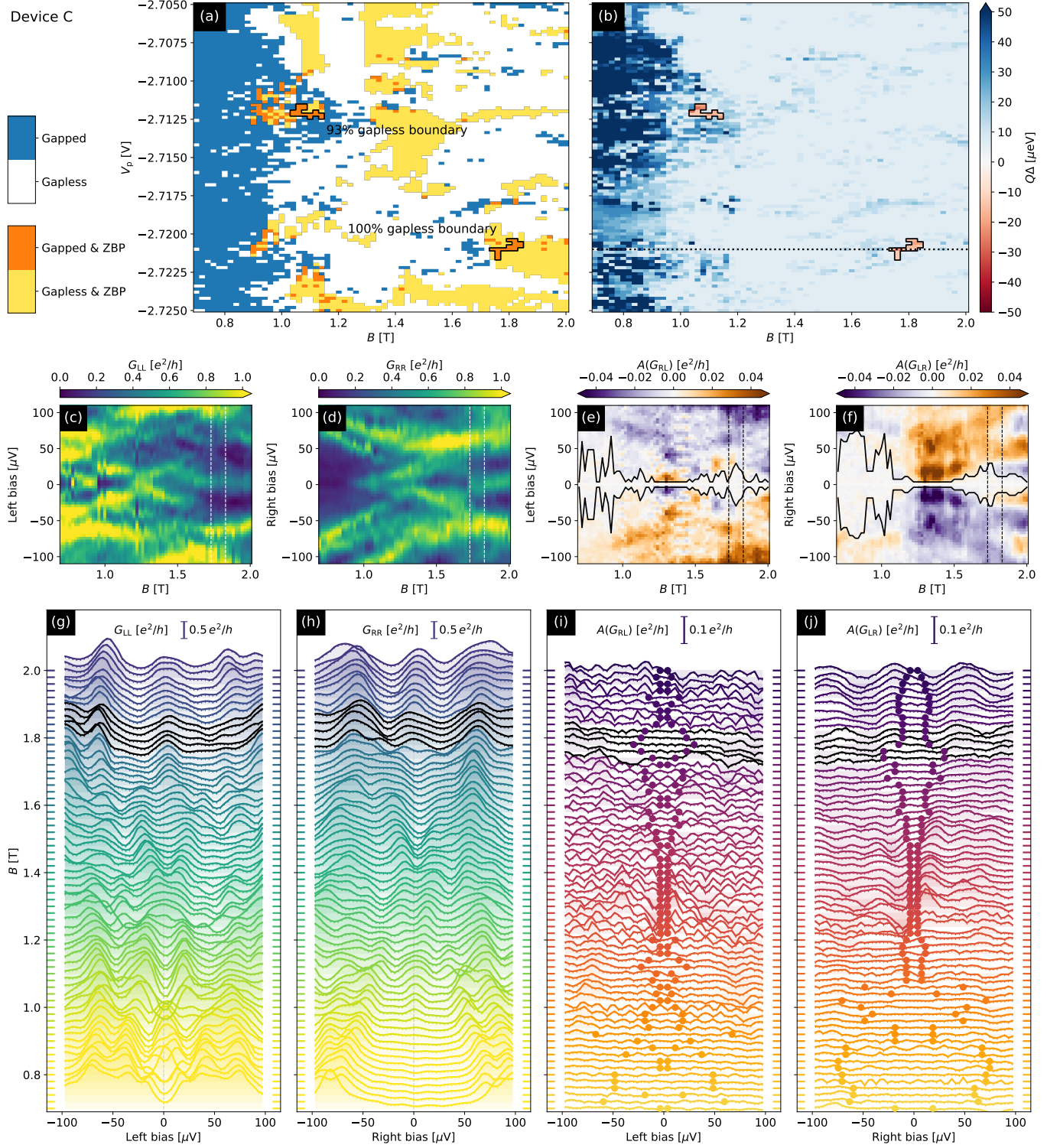


FIG. 15. Stage 2 data for device C. There are two topological regions in the phase diagram. (a) The experimental phase diagram of device C that results from combining the clusters of stable ZBPs at both junctions with the map of the locus of zero/non-zero gap. The boundary of the ROI₂s are interpreted as phase transition lines, consistent with visible gap closures along, respectively, 93% and 100% of them. (b) The experimental phase diagram, showing the trivial/topological phases, which the TGP identifies with the exterior/interior ($Q = \pm 1$) of the ROI₂. The color scale shows the size of the trivial (blue) or topological (red) gap. The protocol assigns maximum topological gaps of 21 μeV and 19 μeV for the top and bottom clusters, respectively. Measured local and antisymmetrized non-local conductances along the horizontal line in panel b at $V_p = -2.721\text{ V}$: (c) G_{LL} , (d) G_{RR} , (e) $A(G_{RL})$, (f) $A(G_{LR})$. The ROI₂ lies between the vertical lines. Panels (g)-(j) are “waterfall” plots representing the same measured data. All data shown in this figure were obtained for left/right $B = 0$ conductances of approximately $0.8e^2/h$ at an above-gap bias voltage of 500 μV . The black curves in panels (e) and (f) and the dots in panels (i) and (j) indicate where the non-local signal drops below a threshold value, as described in the text.

served in our devices.

4.2.1. Additional devices B and C passing the Topological Gap Protocol

The experimental phase diagram for device B is shown in Fig. 14. The TGP assigns this device a maximum topological gap $\Delta_{\text{topo}}^{\text{max}} = 18 \mu\text{eV}$, which is comparable to that of A1 and A3. The lowest B field at which the gap closes is 0.7 T, corresponding to $|g_{\text{eff}}| \approx 4.4$, which is comparable to but smaller than that of device A. The extent of the topological phase is $\delta V_p \approx 1.5 \text{ mV}$ and $\delta B = 0.2 \text{ T}$. On the other hand, Device B's ROI_2 is at significantly lower plunger gate voltage $V_p \approx -2.3655 \text{ V}$ than device A's. (We attribute this to differences in the dielectric that were confirmed by Hall bar measurements.) In addition, the gap closing in device B is more clearly visible in $A(G_{\text{RL}})$ than in $A(G_{\text{LR}})$, and the ZBP has much higher amplitude in G_{LL} than in G_{RR} . Note that there is some evidence that device B is quite clean: it shows Fabry-Pérot oscillations in $A(G_{\text{LR}})$, as shown in Fig. 5. The data is otherwise similar to that obtained from device A.

In Fig. 15, we show data from device C. There are two topological regions in the phase diagram. The TGP assigns maximum topological gaps of $21 \mu\text{eV}$ and $19 \mu\text{eV}$ for the top and bottom regions, respectively. Even taken together, these regions occupy relatively small fraction of the phase diagram. The top cluster is detected at $B = 1.1 \text{ T}$ whereas the bottom one appears at $B \gtrsim 1.8 \text{ T}$. The latter is a relatively high field, but it is consistent with the broad distribution of fields that we find in simulations.

4.2.2. Devices D and E not passing TGP

In Fig. 16, we show data from device D. This device has large regions with stable ZBPs at each end and thus shows a relatively large ROI_1 in the Stage 1 of the TGP. However, in Stage 2 the system appears gapless throughout the region of interest: The induced gap closes and there are no signatures of gap re-opening in the non-local measurements. Since the system appears gapless in non-local conductances it is unclear if the correlated ZBPs correspond to a topological or trivial phase — either the topological gap is too small to be experimentally resolved or we observe a trivial state that couples to both sides because of the long coherence length that is expected in a system with very small gap. The fact that the ZBP is significantly brighter in G_{RR} than in G_{LL} as well as the similarity of finite-bias features in local measurements hints towards the second scenario. In both cases, such a phase would not be suitable for topological quantum computation. This example demonstrates the importance of Stage 2 of the TGP where non-local conductance is measured in order to identify false positives from Stage 1.

Meanwhile, device E does not have any regions with

stable ZBPs at both ends, as may be seen in Fig. 17. The absence of correlations may be due to an inhomogeneous slowly-varying potential along the nanowire. The ZBPs that are seen at one end or the other are very similar to the ZBPs that are seen in devices passing the TGP. However, the ZBP that show up in more than 70% of cutter settings show no stable correlations between the two junctions. They may originate from a trivial Andreev bound states (ABS) crossing zero energy or stable ZBPs, dubbed quasi-MZMs, that appear due to a slowly-varying potential near the junction. Such states do not span over the whole length of the wire. The absence of a large enough cluster of correlated ZBPs causes this device to fail Stage 1 of the TGP.

5. SUMMARY AND DISCUSSION

In the previous sections, we have presented a summary of observed phenomena in gate-defined semiconductor nanowires coupled to a superconductor. We have demonstrated that, when our devices are tuned to the single sub-band regime, they yield data passing the TGP at magnetic fields in the range 1-2 T. We emphasize that our results are reproducible within the same cooldown and between different cooldowns, as we have shown for device A. In summary, our main empirical result is that multiple devices have passed the TGP.

We believe that these measurements represent strong evidence for the observation of a topological superconducting phase supporting MZMs. The TGP has been tested with extensive simulations, correctly distinguishing simulated devices with a topological phase from those without one and correctly distinguishing trivial Andreev bound states from Majorana zero modes. The principal result of our simulations is that there is a $> 98\%$ probability that the TGP will correctly map out the topological phase diagram of a device.

In order to guide incremental progress towards passing the TGP, we relied on our estimates of the material and disorder requirements that gate-defined nanowires must satisfy in order to pass the TGP. We developed designs and fabrication processes capable of meeting these requirements.

In the remainder of this section, we turn to the interpretation of our results.

The stability of the identified topological phase as a function of B and V_p is an important consistency check for our results. For the extracted effective g_{eff} -factor in measurement A1, $\delta B \sim 500 \text{ mT}$ corresponds to a Zeeman energy of $80 \mu\text{eV}$ and, for the calculated lever arm of $\approx 0.06 \text{ eV/V}$, $\delta V_p \sim 1.5 \text{ mV}$ corresponds to a chemical potential shift of $90 \mu\text{eV}$, see Eq. (1). In other words, the phase space extent in field is 3.5 times and the extent in gate voltage is 3.9 times the maximum topological gap of $23 \mu\text{eV}$. Since the topological region has an irregular shape, its area is smaller than the product of these two: the area shown in red in Fig. 9(b) is

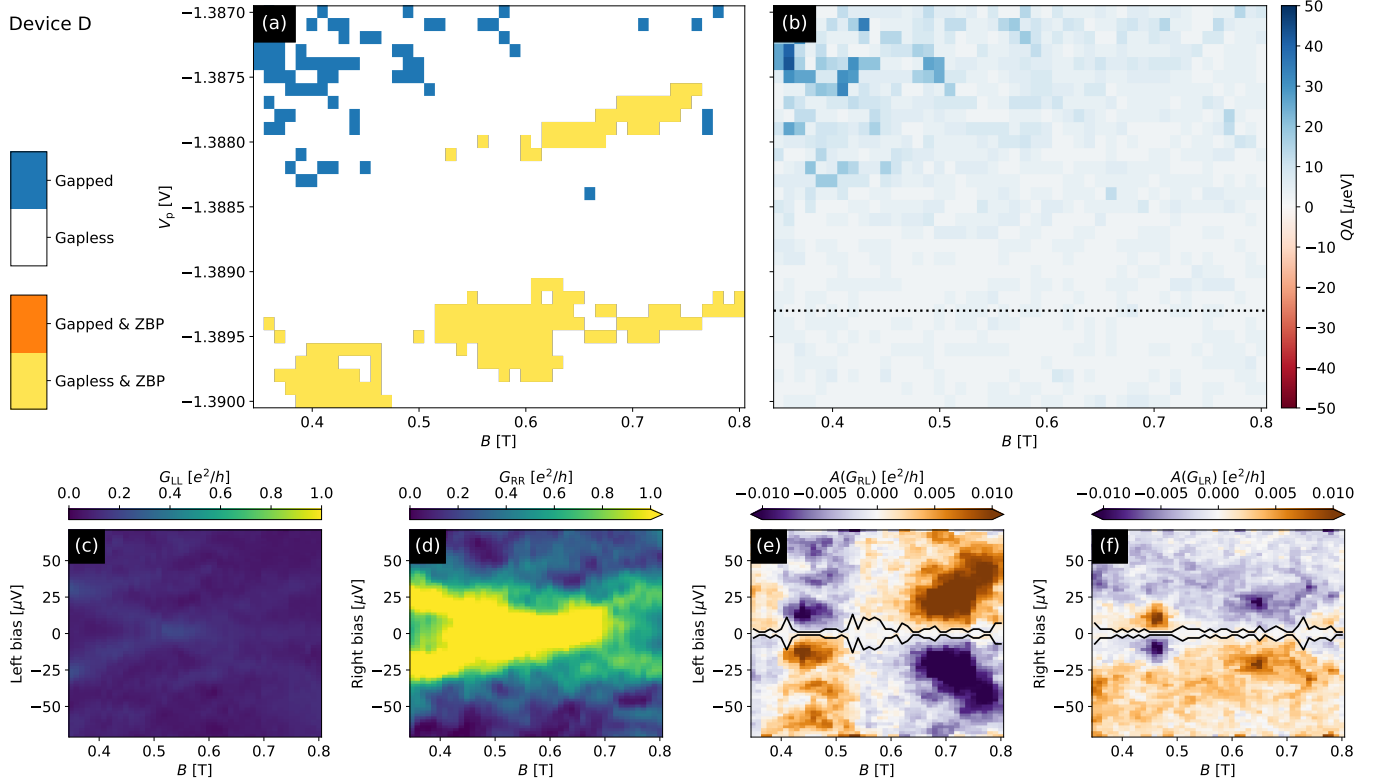


FIG. 16. Stage 2 data for device D. (a) The regions with stable ZBPs at both junctions. The stability of ZBPs is determined by varying the cutter gate settings so that the above gap conductances are 0.6 and $1.0e^2/h$ on the left and 0.2 and $0.4e^2/h$ on the right. (b) The gap as function of B , V_p . It vanishes in the region of interest, so this device fails the TGP. Measured local and antisymmetrized non-local conductances along the horizontal line in panel b at $V_p = -1.3893$ V: (c) G_{LL} , (d) G_{RR} , (e) $A(G_{RL})$, (f) $A(G_{LR})$. The local conductances in panels c and d show ZBPs, but there is no gap re-opening visible in the anti-symmetrized non-local conductances in panels e and f. The cut shown in (c)-(f) is at an above-gap conductance of approximately $0.6e^2/h$ on the left and $0.2e^2/h$ at the right for $B = 0$.

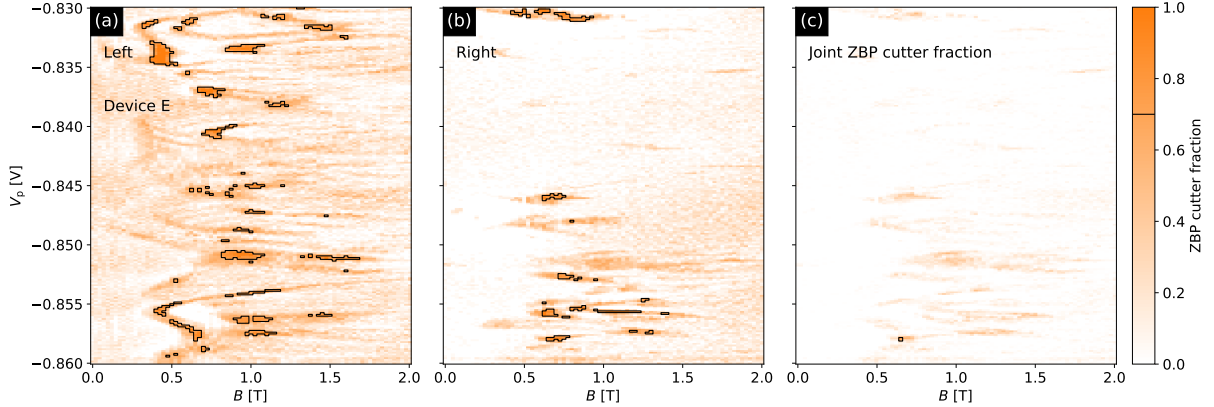


FIG. 17. Stage 1 data for device E. The ZBP probabilities at the (a) left and (b) right junctions as a function B and V_p . As may be seen in panel (c), there is no region that has stable ZBPs at both junctions.

$\approx 0.34 \times 10^{-3} \text{ VT} \approx 6.3 \times (\Delta_{\text{topo}}^{\text{max}})^2$ where $\Delta_{\text{topo}}^{\text{max}} = 23 \mu\text{eV}$ in A1. In measurement A2, we found that the topological region in Fig. 11 extends over a maximum B -field range $\delta B = 500 \text{ mT}$ and a maximum $\delta V_p = 2.5 \text{ mV}$, corresponding, respectively, to energy scales of $80 \mu\text{eV}$ and $150 \mu\text{eV}$. The area of the topological region is \approx

$0.47 \times 10^{-3} \text{ VT} \approx 6.2 \times (\Delta_{\text{topo}}^{\text{max}})^2$, where $\Delta_{\text{topo}}^{\text{max}} = 29 \mu\text{eV}$ in A2. For measurement A3 in Fig. 12, we find a topological region of area $\approx 0.17 \times 10^{-3} \text{ VT} \approx 3.9 \times (\Delta_{\text{topo}}^{\text{max}})^2$ where $\Delta_{\text{topo}}^{\text{max}} = 22 \mu\text{eV}$ in A3. Device B's phase diagram has a topological region of area $\approx 0.074 \times 10^{-3} \text{ VT} \approx 1.75 \times (\Delta_{\text{topo}}^{\text{max}})^2$ where $\Delta_{\text{topo}}^{\text{max}} = 18 \mu\text{eV}$ in B. In device C

in Fig. 15, the area of the bottom topological region is $\approx 0.06 \times 10^{-3} \text{ VT} \approx 1.1(\Delta_{\text{topo}}^{\text{max}})^2$ where $\Delta_{\text{topo}}^{\text{max}} = 19 \mu\text{eV}$. In other words, the observed candidate MZMs are stable with respect to parameter changes larger than the maximum topological gap, which is an intrinsic energy scale of the problem that was determined separately. The observed phase space of the topological phase is consistent with the simulations presented in Fig. 7, where the topological phase has an area $\approx 1.9 \times 10^{-3} \text{ VT} \approx 15.8(\Delta_{\text{topo}}^{\text{max}})^2$, where $\Delta_{\text{topo}}^{\text{max}} = 31 \mu\text{eV}$. In summary, the phase space for the topological phase is roughly as large as we would expect for a maximum topological gap of 20-30 μeV . We note that this is a larger gap than in early measurements of the $\nu = 5/2$ fractional quantum Hall state [109, 110] and further note that the topological gap at $\nu = 5/2$ subsequently increased dramatically with material quality [111, 112].

We now consider other potential explanations of our results. The short answer is that the probability of passing the TGP is less than 2% if a device does not have a topological phase, so any other explanation is extremely unlikely, though not impossible. For an intuitive understanding of why other explanations are unlikely, let us discuss trivial ZBPs. First, we observe that all of our devices have trivial ZBPs, even the ones that pass the TGP. Often, they occur at only one junction, but they sometimes occur at both junctions and they can even be stable both to changes in junction transparency and to changes in B and V_p . For instance, there are stable ZBPs at both junctions in measurement A1 for $1 \text{ T} < B < 2 \text{ T}$ and $V_p \approx -1.173 \text{ V}$, as may be seen in Fig. 9. In device D, there are stable ZBPs at both junctions for $0.5 \text{ T} < B < 0.6 \text{ T}$ and $V_p \approx -1.13895 \text{ V}$, as may be seen in Fig. 15. These are all trivial and fall outside the topological region because the observed bulk transport gap is zero.

Now, let us consider the causes of trivial ZBPs. One possible origin is a slowly-varying potential near the end of a device, which can be caused by certain tunnel barriers. In sufficiently clean devices, this can lead to quasi-MZMs *before* a bulk gap closing, where they are a precursor to the topological phase transition [46–50]. Quasi-MZMs do not appear *after* a gap closing/re-opening. If the bulk gap never re-opens, as in Fig. 20(a)-(d), then quasi-MZMs fail to become MZMs. However, if the bulk gap re-opens, as in Fig. 20(e)-(h), then quasi-MZMs evolve into true MZMs. By design, Stage 2 of the TGP weeds out stable ZBP clusters in which quasi-MZMs don't evolve into true MZMs.

Trivial ZBPs can also be induced by disorder in proximitized semiconductor nanowires with spin-orbit coupling [43–45]. However, this scenario does not entail a gap closing and re-opening in the non-local signal, from which we conclude that it does not apply to devices A, B, and C. ZBPs can also be caused by trivial ABS, which can “accidentally” pass through zero energy. It is very difficult to discern a trivial ABS from an MZM purely from the local conductance spectroscopy, which can be

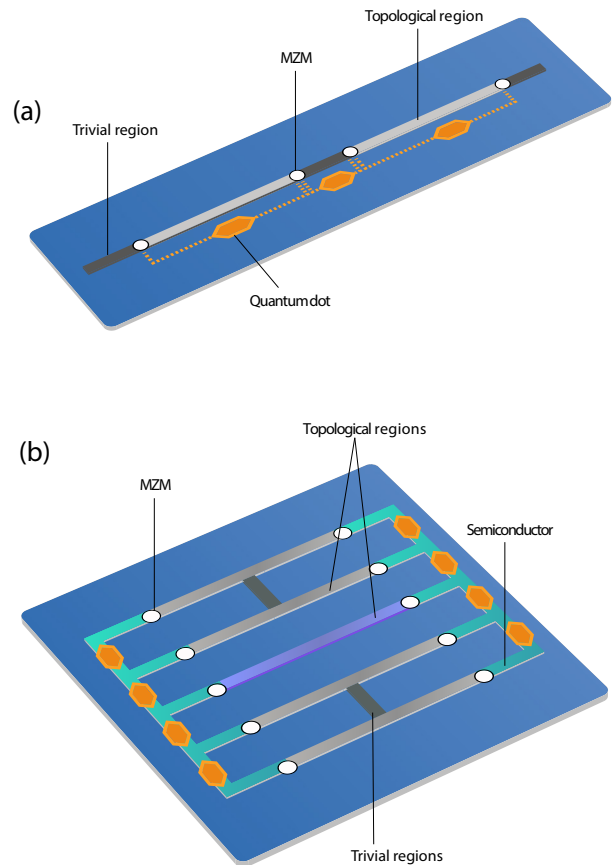


FIG. 18. (a) The linear tetron, a minimal device for performing fusion. The two outer regions must be tuned into the topological phase via the TGP, while the middle section must be in the trivial phase. This results in a device with four MZMs. (b) Two two-sided tetrons, with which measurement-based braiding can be performed. There are 5 topological sections. The middle (purple) one is a coherent link that is used for connecting the left and right of the two tetrons.

virtually identical. However, as in the case of disorder-induced ZBPs, a trivial ABS need not be accompanied by a gap closing and re-opening in the non-local signal.

A gap closing/re-opening could be caused by the orbital effects of the magnetic field. When half a flux quantum is threaded through the effective cross-sectional area of the device, the proximity effect is suppressed, and the gap closes. It re-opens when the flux increases still further, closing a second time when $3/2$ flux quanta thread the active region. For device A, we expect a gap closing due to orbital effects at $\gtrsim 2.5 \text{ T}$. The observed gap closing is at much lower fields. Crucially, a gap closing due to orbital effects would be weakly-dependent on the gate voltage, as illustrated by the simulated phase diagram of a clean system in Fig. 3, where the first closing due to orbital effects is a wide, nearly vertical white bar at $B \approx 2.5 \text{ T}$ that intersects the topological lobes at $V_p \approx -0.7 \text{ V}$ and $V_p \approx -0.9 \text{ V}$. We find similar behavior in the simulations that we used to test the TGP,

which include disorder. On the other hand, as may be seen in Fig. 11, the gap closing that is observed in device A is strongly dependent on the gate voltage: at $V_p \approx -1.407$ V, the gap closes at $B \approx 0.6$ T, but at $V_p \approx -1.398$ V, it is still open at $B = 2$ T. Hence, an explanation relying on the orbital effect of the magnetic field is not consistent with either the B field value or the V_p -dependence of the observed gap closing/re-opening.

Of course, it is conceivable that the bulk gap closes and re-opens accidentally and that trivial ZBPs also accidentally occur for the same B and V_p . But to pass the TGP, the accidental closing would have to occur over an entire curve in the (B, V_p) phase space and, moreover, the trivial ZBPs would have to persist over the enclosed region. Of course, we cannot rule this out completely. However, as we have seen from our simulations, the probability for such a false positive outcome of the TGP is $< 2\%$. Thus, while the preceding qualitative considerations help us develop intuition for why neither trivial ABS nor orbital gap closings lead to a false positive outcome for the TGP, it is far more important that we have found no false positives after testing the TGP against 61 different device simulations, which implies low probability that devices A-C do not have a topological phase.

6. LOOKING AHEAD

A reliable process for tuning devices into the topological phase is an essential step on the journey to topological quantum computation, which relies on the fusion and braiding of anyons. Networks of such wires can be assembled into a many-qubit device, and this protocol can be used to tune each wire within a qubit into the topological phase. The linear tetron qubit [113, 114] is a minimal device for performing two non-commuting fusion operations;⁵ it is shown schematically in Fig. 18(a). There are two outer topological sections, separated by a trivial section. Fusion outcomes are measured by coupling quantum dots to different pairs of MZMs, giving us a direct experimental measurement of a topological invariant of the state. The parameter space of such a device is simply too large to explore in the hope of finding a suitable operating point unless the nanowire is tuned into a configuration in which the two outer sections are in the topological phase, which can be achieved using the TGP. Coherent manipulation of the encoded quantum state, for example through measurement-based implementations of braiding transformations [120, 121], requires an even more complex device, as shown in Fig. 18(b). Despite the even larger parameter space, these devices can be tuned using the TGP. Continued improvement in simulation, growth, fabrication, and measurement capabilities will be required to achieve the topological gap required for such coherent operations.

⁵ See Refs. 115–119 for related alternate qubit designs.

ACKNOWLEDGMENTS

We thank Greg Boebinger, Sankar Das Sarma, Michel Devoret, Klaus Ensslin, Leonid Glazman, Bert Halperin, Kam Moler, and Dale van Harlingen for extensive discussions. We are grateful to Edward Lee and Todd Ingalls for their assistance with figures. We thank Leo Kouwenhoven for helpful comments on a previous version of this manuscript.

Correspondence and requests for materials should be addressed to Chetan Nayak (cnayak@microsoft.com).

[†]Morteza Aghaee, Arun Akkala, Zulfi Alam, Rizwan Ali, Alejandro Alcaraz Ramirez, Mariusz Andrzejczuk, Andrey E Antipov, Pavel Aseev, Mikhail Astafev, Bela Bauer, Jonathan Becker, Srini Boddapati, Frenk Boekhout, Jouri Bommer, Esben Bork Hansen, Tom Bosma, Leo Bourdet, Samuel Boutin, Philippe Caroff, Lucas Casparis, Maja Cassidy, Anna Wulf Christensen, Noah Clay, William S Cole, Fabiano Corsetti, Ajuan Cui, Paschalis Dalampiras, Anand Dokania, Gijs de Lange, Michiel de Moor, Juan Carlos Estrada Saldaña, Saeed Fallahi, Zahra Heidarnia Fathabad, John Gamble, Geoff Gardner, Deshan Govender, Flavio Griggio, Ruben Grigoryan, Sergei Gronin, Jan Gukelberger, Sebastian Heedt, Jesús Herranz Zamorano, Samantha Ho, Ulrik Laurens Holgaard, William Hvidtfelt Padkær Nielsen, Henrik Ingerslev, Linda Johansson, Jeffrey Jones, Ray Kallagher, Farhad Karimi, Torsten Karzig, Evelyn King, Maren Elisabeth Kloster, Christina Knapp, Dariusz Kocon, Jonne Koski, Pasi Kostamo, Peter Krogstrup, Mahesh Kumar, Tom Laeven, Thorvald Larsen, Kongyi Li, Tyler Lindemann, Julie Love, Roman Lutchyn, Michael Manfra, Elvedin Memisevic, Chetan Nayak, Bas Nijholt, Morten Hannibal Madsen, Signe Markussen, Esteban Martinez, Robert McNeil, Andrew Mulally, Jens Nielsen, Anne Nurmohamed, Eoin O’Farrell, Keita Otani, Sebastian Pauka, Karl Petersson, Luca Petit, Dima Pikulin, Frank Preiss, Marina Quintero Perez, Katrine Rasmussen, Mohana Rajpalke, Davyd Razmadze, Outi Reentila, David Reilly, Richard Rouse, Ivan Sadovskyy, Lauri Sainiemi, Sydney Schreppler, Vadim Sidorkin, Amrita Singh, Shilpi Singh, Sarat Sinha, Patrick Sohr, Tomaš Stankevič, Lieuwe Stek, Henri Suominen, Judith Suter, Vicky Svidenko, Sam Teicher, Mine Temuerhan, Nivetha Thiyagarajah, Raj Tholapi, Mason Thomas, Emily Toomey, Shivendra Upadhyay, Ivan Urban, Saulius Vaitiekėnas, Kevin Van Hoogdalem, Dmitrii V. Viazmitinov, Steven Waddy, David Van Woerkom, Dominik Vogel, John Watson, Joseph Weston, Georg W. Winkler, Chung Kai Yang, Sean Yau, Daniel Yi, Emrah Yucelen, Alex Webster, Roland Zeisel, Ruichen Zhao.

Appendix A: Electrostatic calibration from Hall bars

Each of the topological gap devices described in the main text is accompanied by a Hall bar device subject to the same growth and fabrication processes; this Hall bar enables a characterization of the bulk material quality. The full density dependence of the Hall mobility has been widely used previously to identify and quantify dominant scattering mechanisms in 2DEGs [97, 122–130]. In particular, across all samples, the

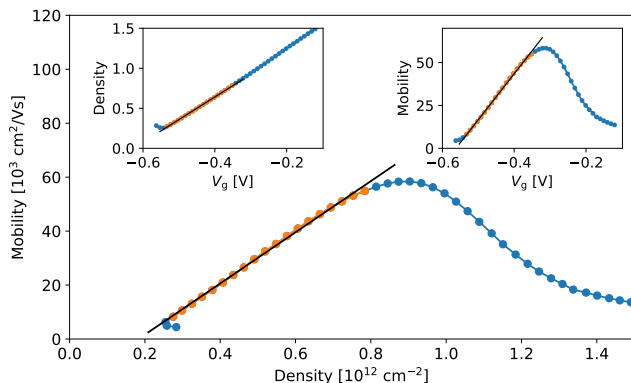


FIG. 19. Measured density and mobility vs. gate voltage (as well as mobility vs. density) from a Hall bar proximate to device A. Orange points indicate the low-density data used in the fit. Solid lines are the simulation result corresponding to the most-probable impurity density and dielectric permittivity.

low-density mobility rapidly increases with increasing density, consistent with the mobility being dominated there by scattering from the long-range Coulomb potential of remote impurities.

In our simulations, we calculate (i) the gate-voltage dependence of carrier density $n(V_g)$ for a 2DEG in our materials stack in a standard Schrödinger-Poisson framework; and (ii) the remote-impurity-limited mobility $\mu(V_g)$ in the Boltzmann-Born formalism. Both of these functions are parameterized by the density and location of impurities, and an effective composite dielectric permittivity. These parameters are used to *simultaneously* fit the model traces to experimental data. As mentioned in the main text, our best fits to density and mobility measurements over a variety of samples suggested a simplification in which an effective 2D impurity density $n_{2D,int}$ is placed in an “impurity layer” at the interface between the barrier and the gate dielectric. Small changes in the position or width of the impurity layer can be compensated by tuning the impurity density, but large changes modify the overall density dependence of the mobility and result in poor fits. Therefore, the values of charge impurity density that we quote here depend on the disorder model employed, with the goal of this model being to provide a *consistent* description of the impact of fixed charges on *both* the Hall mobility and TGP measurements.

Fig. 19 shows a representative example measurement of mobility versus density for the Hall bar proximate to device A (note that the low-density upturn in $n(V_g)$ and non-single-valued $\mu(V_g)$ arise due to a measurement artifact and these points are excluded from the fitting). The solid black lines represent our point estimate traces corresponding to the most-probable values of the effective impurity density (here, the value $n_{2D,int} = 2.7 \times 10^{12} \text{cm}^{-2}$) and effective dielectric permittivity.

Using similar analysis, we extracted the corresponding effective charged impurity densities at the interface with the dielectric for devices B-E yielding $1.1 \times 10^{12} \text{cm}^{-2}$, $1.0 \times 10^{12} \text{cm}^{-2}$, $3.1 \times 10^{12} \text{cm}^{-2}$, $3.0 \times 10^{12} \text{cm}^{-2}$, respectively.

Appendix B: Simulated disorder realizations that fail the Topological Gap Protocol

As noted in Sec. 3.2, out of 38 different simulated disorder realizations for a narrow device with a $3 \mu\text{m}$ long central section and $n_{2D,int} = 2.4 \times 10^{12} \text{cm}^{-2}$ at $T = 0$, there were realizations that failed the TGP. The example that we explored in some detail in Sec. 3.2, which we called realization 1, is one of the realizations that passed both Stages of the protocol. In this appendix, we will show additional simulated data, obtained for different disorder realizations *R2* and *R3*, that fail the TGP at different stages.

We first return to disorder realization R1 but, for the sake of comparison with the data shown in Fig. 7, we also present trivial ZBPs seen at a different value of V_p . In Fig. 20(a-d), we have bias-field scans at $V_p = -1.36575 \text{V}$. In Fig. 20(e-h), we reproduce the corresponding scans at $V_p = -1.37275 \text{V}$ which were previously shown in Fig. 7. In panels (a) and (b), Andreev bound states appear before an apparent gap closing in the local conductance. The bound state in panel (a) is brighter than the one in panel (b), while the apparent gap closing is more visible in panel (b) and is not visible in panel (a). After the apparent gap closing, the Andreev bound states stick to zero energy. Very similar local conductance spectra are shown in panels (e) and (f). From the local conductances, it is very difficult to distinguish the physics observed in Fig. 20(a,b) at $V_p = -1.36575 \text{V}$ from that observed in Fig. 20(e,f) at $V_p = -1.37275 \text{V}$. However, the non-local conductance data in panels (c) and (d) clearly show that the system is gapless at $V_p = -1.36575 \text{V}$ over the range of B field values at which there are ZBPs in Fig. 20(a,b) and panels (g) and (h) show that the system is gapped at $V_p = -1.37275 \text{V}$ over the range of B field values at which there are ZBPs in Fig. 20(e,f). Moreover, the topological indicator is $+1$ at $V_p = -1.36575 \text{V}$ while it is -1 at $V_p = -1.37275 \text{V}$, as may be seen in Fig. 7(a). Thus, the ZBPs in Fig. 20(a,b) are trivial, even though they look very similar to the topological ones in Fig. 20(e,f). For this reason, we emphasize that local conductance measurements alone cannot distinguish an MZM from a trivial Andreev bound state. However, the TGP can.

In Fig. 21, we present another disorder realization, which we call R2. This is one of the realizations that passed Stage 1 but failed Stage 2. There are stable ZBPs at both junctions at $V_p = -1.3395 \text{V}$, as may be seen in Fig. 21(c,d). However, the non-local conductances in Fig. 21(e,f) yield zero gap. In fact, the system is gapless over most of the scanned region, so this simulated transport data does not pass Stage 2 of the TGP. This example once again reinforces the fact that local measurements alone cannot detect a topological phase.

In Fig. 22, we present another disorder realization, which we call R3. This is one of the nine realizations that did not pass Stage 1. There are fairly large regions in the phase diagram with stable ZBPs at the right junction but they do not overlap with the much smaller regions with stable ZBPs at the left junction. As a result, there is no overlapping region in V_p and B space that has stable ZBPs at both junctions, as may be seen in panel (c). This typically occurs when the potential is non-uniform along the wire.

We emphasize, however, that R2 and R3 were drawn from the same probability distribution as R1. Although they have the same average disorder levels, the individual disorder realizations in R1-R3 lead to rather different phase diagrams. Although, at $3 \mu\text{m}$, the devices are rather long, their phase

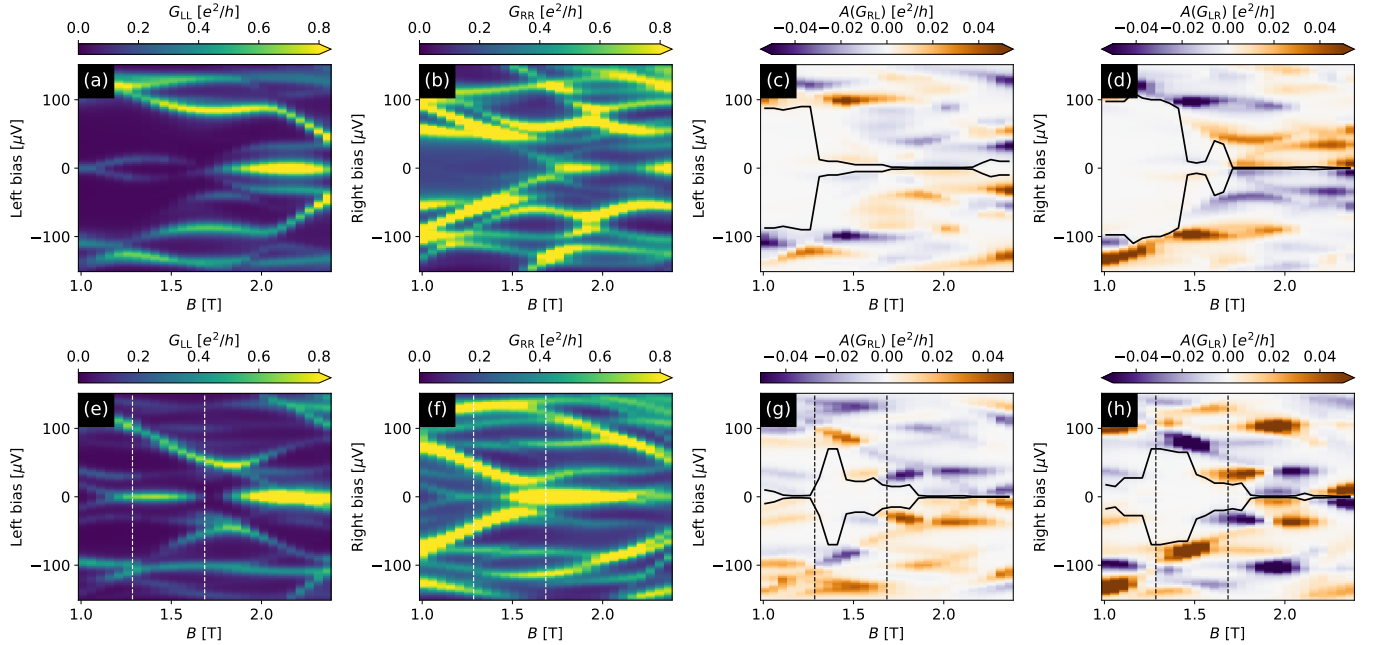


FIG. 20. Simulated bias-field scans at $V_p = -1.36575$ V [panels (a)-(d)] and $V_p = -1.37275$ V [panels (e)-(h), copy of Fig. 7(c)-(f)] for disorder realization R1 in a narrow, $3\ \mu\text{m}$ long wire with $n_{2D,\text{int}} = 2.4 \times 10^{12}\text{cm}^{-2}$. The scans in panels (a)-(d) show conductances from the non-topological region (outside of ROI_2) whereas scans (e)-(h) intersect the ROI_2 , which lies between the vertical lines. As may be seen by comparing panels (a), (b) and (e), (f), the local conductances are similar, but the non-local conductances in panels (c), (d) lack a clear transport gap re-opening, distinguishing them from (g), (h).

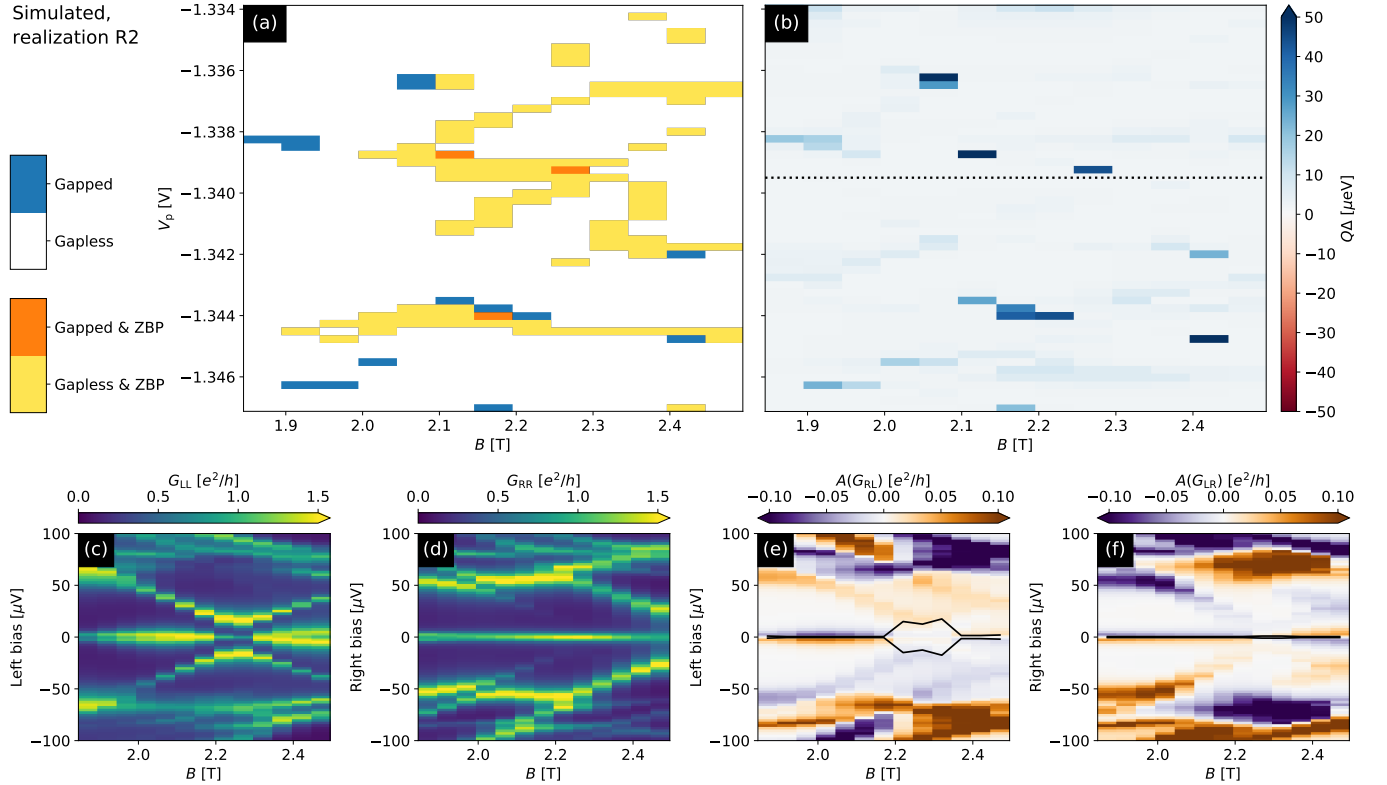


FIG. 21. Stage 2 data for realization R2 at zero temperature. (a) The regions with stable ZBPs at both junctions. (b) The gap as function of B and V_p . It vanishes in the region of interest, so this device fails the TGP. (c)-(f) Local and antisymmetrized non-local conductances at $V_p = -1.3395$ V. The local conductances in panels (c) and (d) show ZBPs, but there is no gap re-opening visible in the antisymmetrized non-local conductances in panels (e) and (f).

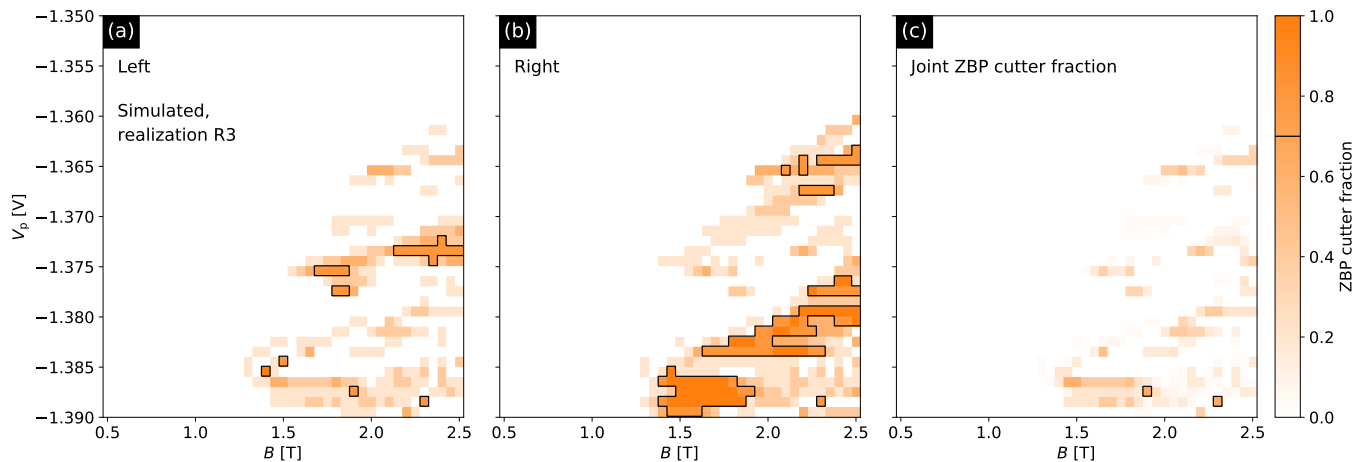


FIG. 22. Stage 1 data for disorder realization R3 at zero temperature. The ZBP probabilities at the (a) left and (b) right junctions as a function B and V_p . There is a stable ZBP at right junction but no stable ZBPs at the opposite end. As a result, there is no region that has stable ZBPs at both junctions at the same B and V_p , see panel (c). Thus, this data does not pass Stage 1 of the TGP.

diagrams are not self-averaging for this disorder level. Hence, it is not surprising that we find different experimental phase

diagrams for devices that have nominally similar disorder levels.

-
- [1] A. Y. Kitaev, Fault-tolerant quantum computation by anyons, *Ann. Phys.* **303**, 2 (2003), [quant-ph/9707021](#).
- [2] M. H. Freedman, P/NP , and the quantum field computer, *Proc. Natl. Acad. Sci. USA* **95**, 98 (1998).
- [3] C. Nayak, S. H. Simon, A. Stern, M. Freedman, and S. Das Sarma, Non-Abelian anyons and topological quantum computation, *Rev. Mod. Phys.* **80**, 1083 (2008), [arXiv:0707.1889](#).
- [4] J. Alicea, New directions in the pursuit of Majorana fermions in solid state systems, *Rep. Prog. Phys.* **75**, 076501 (2012), [arXiv:1202.1293](#).
- [5] S. D. Sarma, M. Freedman, and C. Nayak, Majorana zero modes and topological quantum computation, *npj Quantum Inf.* **1**, 1 (2015).
- [6] D. Aasen, M. Hell, R. V. Mishmash, A. Higginbotham, J. Danon, M. Leijnse, T. S. Jespersen, J. A. Folk, C. M. Marcus, K. Flensberg, and J. Alicea, Milestones toward Majorana-based quantum computing, *Phys. Rev. X* **6**, 031016 (2016), [arXiv:1511.05153](#).
- [7] V. von Burg, G. H. Low, T. Häner, D. S. Steiger, M. Reiher, M. Roetteler, and M. Troyer, Quantum computing enhanced computational catalysis, *Phys. Rev. Research* **3**, 033055 (2021).
- [8] D. I. Pikulin, B. van Heck, T. Karzig, E. A. Martinez, B. Nijholt, T. Laeven, G. W. Winkler, J. D. Watson, S. Heedt, M. Temurhan, V. Svidenko, R. M. Lutchyn, M. Thomas, G. de Lange, L. Casparis, and C. Nayak, Protocol to identify a topological superconducting phase in a three-terminal device (2021), [arXiv:2103.12217](#).
- [9] A. Y. Kitaev, Unpaired Majorana fermions in quantum wires, *Phys.-Usp.* **44**, 31 (2001), [arXiv:cond-mat/0010440](#).
- [10] J. D. Sau, R. M. Lutchyn, S. Tewari, and S. Das Sarma, Generic new platform for topological quantum computation using semiconductor heterostructures, *Phys. Rev. Lett.* **104**, 040502 (2010), [arXiv:0907.2239](#).
- [11] R. M. Lutchyn, J. D. Sau, and S. Das Sarma, Majorana Fermions and a topological phase transition in semiconductor-superconductor heterostructures, *Phys. Rev. Lett.* **105**, 077001 (2010), [arXiv:1002.4033](#).
- [12] Y. Oreg, G. Refael, and F. von Oppen, Helical liquids and Majorana bound states in quantum wires, *Phys. Rev. Lett.* **105**, 177002 (2010), [arXiv:1003.1145](#).
- [13] A. Kitaev, Anyons in an exactly solved model and beyond, *Ann. Phys.* **321**, 2 (2006), [arXiv:cond-mat/0506438](#).
- [14] P. Bonderson, Measuring topological order, *Phys. Rev. Research* **3**, 033110 (2021).
- [15] C. de C. Chamon, D. E. Freed, S. A. Kivelson, S. L. Sondhi, and X. G. Wen, Two point-contact interferometer for quantum Hall systems, *Phys. Rev. B* **55**, 2331 (1997).
- [16] E. Fradkin, C. Nayak, A. Tsvetlik, and F. Wilczek, A Chern-Simons effective field theory for the Pfaffian quantum Hall state, *Nucl. Phys. B* **516**, 704 (1998), [arXiv:cond-mat/9711087](#).
- [17] P. Bonderson, A. Kitaev, and K. Shtengel, Detecting non-Abelian statistics in the $\nu = 5/2$ fractional quantum Hall state, *Phys. Rev. Lett.* **96**, 016803 (2006), [arXiv:cond-mat/0508616](#).
- [18] A. Stern and B. I. Halperin, Proposed experiments to probe the non-Abelian $\nu = 5/2$ quantum Hall state, *Phys. Rev. Lett.* **96**, 016802 (2006), [arXiv:cond-mat/0508447](#).
- [19] R. L. Willett, L. N. Pfeiffer, and K. W. West, Alternation and interchange of $e/4$ and $e/2$ period interference oscillations consistent with filling factor $5/2$ non-Abelian quasiparticles, *Phys. Rev. B* **82**, 205301 (2010),

- arXiv:0911.0345.
- [20] C. Grenier, R. Hervé, G. Fève, and P. Degiovanni, Electron quantum optics in quantum Hall edge channels, *Modern Physics Letters B* **25**, 1053 (2011), arXiv:1102.0466.
- [21] M. Banerjee, M. Heiblum, V. Umansky, D. E. Feldman, Y. Oreg, and A. Stern, Observation of half-integer thermal Hall conductance, *Nature* **559**, 205 (2018).
- [22] J. Nakamura, S. Liang, G. C. Gardner, and M. J. Manfra, Direct observation of anyonic braiding statistics, *Nat. Phys.* **16**, 931 (2020).
- [23] K. T. Law, P. A. Lee, and T. K. Ng, Majorana fermion induced resonant Andreev reflection, *Phys. Rev. Lett.* **103**, 237001 (2009).
- [24] J. D. Sau, S. Tewari, R. M. Lutchyn, T. D. Stanescu, and S. Das Sarma, Non-Abelian quantum order in spin-orbit-coupled semiconductors: Search for topological Majorana particles in solid-state systems, *Phys. Rev. B* **82**, 214509 (2010).
- [25] K. Flensberg, Tunneling characteristics of a chain of Majorana bound states, *Phys. Rev. B* **82**, 180516 (2010).
- [26] M. Wimmer, A. R. Akhmerov, J. P. Dahlhaus, and C. W. J. Beenakker, Quantum point contact as a probe of a topological superconductor, *New J. Phys.* **13**, 053016 (2011).
- [27] T. D. Stanescu, R. M. Lutchyn, and S. Das Sarma, Majorana fermions in semiconductor nanowires, *Phys. Rev. B* **84**, 144522 (2011), arXiv:1106.3078.
- [28] L. Fidkowski, J. Alicea, N. H. Lindner, R. M. Lutchyn, and M. P. A. Fisher, Universal transport signatures of Majorana fermions in superconductor-Luttinger liquid junctions, *Phys. Rev. B* **85**, 245121 (2012).
- [29] V. Mourik, K. Zuo, S. M. Frolov, S. R. Plissard, E. P. A. M. Bakkers, and L. P. Kouwenhoven, Signatures of Majorana fermions in hybrid superconductor-semiconductor nanowire devices, *Science* **336**, 1003 (2012), arXiv:1204.2792.
- [30] A. Das, Y. Ronen, Y. Most, Y. Oreg, M. Heiblum, and H. Shtrikman, Zero-bias peaks and splitting in an Al-InAs nanowire topological superconductor as a signature of Majorana fermions, *Nat. Phys.* **8**, 887 (2012), arXiv:1205.7073.
- [31] M. T. Deng, C. L. Yu, G. Y. Huang, M. Larsson, P. Caroff, and H. Q. Xu, Anomalous zero-bias conductance peak in a Nb-InSb nanowire-Nb hybrid device, *Nano Lett.* **12**, 6414 (2012), arXiv:1204.4130.
- [32] A. D. K. Finck, D. J. Van Harlingen, P. K. Mohseni, K. Jung, and X. Li, Anomalous modulation of a zero-bias peak in a hybrid nanowire-superconductor device, *Phys. Rev. Lett.* **110**, 126406 (2013).
- [33] H. O. H. Churchill, V. Fatemi, K. Grove-Rasmussen, M. T. Deng, P. Caroff, H. Q. Xu, and C. M. Marcus, Superconductor-nanowire devices from tunneling to the multichannel regime: Zero-bias oscillations and magnetoconductance crossover, *Phys. Rev. B* **87**, 241401 (2013), arXiv:1303.2407.
- [34] M. T. Deng, S. Vaitiekėnas, E. B. Hansen, J. Danon, M. Leijnse, K. Flensberg, J. Nygård, P. Krogstrup, and C. M. Marcus, Majorana bound state in a coupled quantum-dot hybrid-nanowire system, *Science* **354**, 1557 (2016).
- [35] F. Nichele, A. C. C. Drachmann, A. M. Whiticar, E. C. T. O'Farrell, H. J. Suominen, A. Fornieri, T. Wang, G. C. Gardner, C. Thomas, A. T. Hatke, P. Krogstrup, M. J. Manfra, K. Flensberg, and C. M. Marcus, Scaling of Majorana zero-bias conductance peaks, *Phys. Rev. Lett.* **119**, 136803 (2017).
- [36] S. Vaitiekėnas, M.-T. Deng, J. Nygård, P. Krogstrup, and C. M. Marcus, Effective g factor of subgap states in hybrid nanowires, *Phys. Rev. Lett.* **121**, 037703 (2018).
- [37] M. W. A. de Moor, J. D. S. Bommer, D. Xu, G. W. Winkler, A. E. Antipov, A. Bargerbos, G. Wang, N. van Loo, R. L. M. O. het Veld, S. Gazibegovic, D. Car, J. A. Logan, M. Pendharkar, J. S. Lee, E. P. A. M. Bakkers, C. J. Palmstrøm, R. M. Lutchyn, L. P. Kouwenhoven, and H. Zhang, Electric field tunable superconductor-semiconductor coupling in Majorana nanowires, *New J. Phys.* **20**, 103049 (2018).
- [38] R. M. Lutchyn, E. P. A. M. Bakkers, L. P. Kouwenhoven, P. Krogstrup, C. M. Marcus, and Y. Oreg, Majorana zero modes in superconductor-semiconductor heterostructures, *Nat. Rev. Mater.* **3**, 52 (2018).
- [39] G. L. R. Anselmetti, E. A. Martinez, G. C. Ménard, D. Puglia, F. K. Malinowski, J. S. Lee, S. Choi, M. Pendharkar, C. J. Palmstrøm, C. M. Marcus, L. Casparis, and A. P. Higginbotham, End-to-end correlated subgap states in hybrid nanowires, *Phys. Rev. B* **100**, 205412 (2019).
- [40] H. Zhang, M. W. A. de Moor, J. D. S. Bommer, D. Xu, G. Wang, N. van Loo, C.-X. Liu, S. Gazibegovic, J. A. Logan, D. Car, R. L. M. O. h. Veld, P. J. van Veldhoven, S. Koelling, M. A. Verheijen, M. Pendharkar, D. J. Pennachio, B. Shojaei, J. S. Lee, C. J. Palmstrøm, E. P. A. M. Bakkers, S. D. Sarma, and L. P. Kouwenhoven, Large zero-bias peaks in InSb-Al hybrid semiconductor-superconductor nanowire devices (2021), arXiv:2101.11456.
- [41] S. Vaitiekėnas, G. W. Winkler, B. van Heck, T. Karzig, M.-T. Deng, K. Flensberg, L. I. Glazman, C. Nayak, P. Krogstrup, R. M. Lutchyn, and C. M. Marcus, Flux-induced topological superconductivity in full-shell nanowires, *Science* **367**, eaav3392 (2020).
- [42] A. Banerjee, O. Lesser, M. A. Rahman, H. R. Wang, M. R. Li, A. Kringhøj, A. M. Whiticar, A. C. C. Drachmann, C. Thomas, T. Wang, M. J. Manfra, E. Berg, Y. Oreg, A. Stern, and C. M. Marcus, Signatures of a topological phase transition in a planar Josephson junction (2022).
- [43] D. Bagrets and A. Altland, Class D spectral peak in Majorana quantum wires, *Phys. Rev. Lett.* **109**, 227005 (2012), arXiv:1206.0434.
- [44] D. I. Pikulin, J. P. Dahlhaus, M. Wimmer, H. Schomerus, and C. W. J. Beenakker, A zero-voltage conductance peak from weak antilocalization in a Majorana nanowire, *New J. Phys.* **14**, 125011 (2012).
- [45] H. Pan and S. Das Sarma, On-demand large conductance in trivial zero-bias tunneling peaks in Majorana nanowires, *Phys. Rev. B* **105**, 115432 (2022).
- [46] E. Prada, P. San-Jose, and R. Aguado, Transport spectroscopy of NS nanowire junctions with Majorana fermions, *Phys. Rev. B* **86**, 180503 (2012), arXiv:1203.4488.
- [47] G. Kells, D. Meidan, and P. W. Brouwer, Near-zero-energy end states in topologically trivial spin-orbit coupled superconducting nanowires with a smooth confinement, *Phys. Rev. B* **86**, 100503 (2012).
- [48] T. D. Stanescu and S. Tewari, Nonlocality of zero-bias anomalies in the topologically trivial phase of Majorana

- wires, *Phys. Rev. B* **89**, 220507 (2014).
- [49] C.-X. Liu, J. D. Sau, T. D. Stanescu, and S. Das Sarma, Andreev bound states versus Majorana bound states in quantum dot-nanowire-superconductor hybrid structures: Trivial versus topological zero-bias conductance peaks, *Phys. Rev. B* **96**, 075161 (2017).
- [50] H. Pan, C.-X. Liu, M. Wimmer, and S. Das Sarma, Quantized and unquantized zero-bias tunneling conductance peaks in Majorana nanowires: Conductance below and above $2e^2/h$, *Phys. Rev. B* **103**, 214502 (2021).
- [51] E. J. H. Lee, X. Jiang, R. Aguado, G. Katsaros, C. M. Lieber, and S. De Franceschi, Zero-bias anomaly in a nanowire quantum dot coupled to superconductors, *Phys. Rev. Lett.* **109**, 186802 (2012), arXiv:1207.1259.
- [52] C. Reeg, O. Dmytruk, D. Chevallerier, D. Loss, and J. Klinovaja, Zero-energy Andreev bound states from quantum dots in proximitized Rashba nanowires, *Phys. Rev. B* **98**, 245407 (2018).
- [53] W. Yu, R. Haenel, M. A. Rodriguez, S. R. Lee, F. Zhang, M. Franz, D. I. Pikulin, and W. Pan, Zero-bias conductance peak in Dirac semimetal-superconductor devices, *Phys. Rev. Research* **2**, 032002 (2020).
- [54] E. J. H. Lee, X. Jiang, M. Houzet, R. Aguado, C. M. Lieber, and S. D. Franceschi, Spin-resolved Andreev levels and parity crossings in hybrid superconductor-semiconductor nanostructures, *Nat. Nanotechnol.* **9**, 79 (2013).
- [55] H. J. Suominen, M. Kjaergaard, A. R. Hamilton, J. Shabani, C. J. Palmström, C. M. Marcus, and F. Nichele, Zero-energy modes from coalescing Andreev states in a two-dimensional semiconductor-superconductor hybrid platform, *Phys. Rev. Lett.* **119**, 176805 (2017).
- [56] H. Pan, W. S. Cole, J. D. Sau, and S. Das Sarma, Generic quantized zero-bias conductance peaks in superconductor-semiconductor hybrid structures, *Phys. Rev. B* **101**, 024506 (2020).
- [57] N. Read and D. Green, Paired states of fermions in two dimensions with breaking of parity and time-reversal symmetries and the fractional quantum Hall effect, *Phys. Rev. B* **61**, 10267 (2000).
- [58] A. E. Antipov, A. Bargerbos, G. W. Winkler, B. Bauer, E. Rossi, and R. M. Lutchyn, Effects of gate-induced electric fields on semiconductor Majorana nanowires, *Phys. Rev. X* **8**, 031041 (2018).
- [59] G. W. Winkler, A. E. Antipov, B. van Heck, A. A. Soluyanov, L. I. Glazman, M. Wimmer, and R. M. Lutchyn, Unified numerical approach to topological semiconductor-superconductor heterostructures, *Phys. Rev. B* **99**, 245408 (2019).
- [60] L. Fu and C. L. Kane, Superconducting proximity effect and Majorana fermions at the surface of a topological insulator, *Phys. Rev. Lett.* **100**, 096407 (2008), arXiv:0707.1692.
- [61] L. Fu and C. L. Kane, Josephson current and noise at a superconductor/quantum-spin-Hall-insulator/superconductor junction, *Phys. Rev. B* **79**, 161408(R) (2009).
- [62] J. Alicea, Majorana fermions in a tunable semiconductor device, *Phys. Rev. B* **81**, 125318 (2010).
- [63] J. D. Sau, S. Tewari, R. M. Lutchyn, T. D. Stanescu, and S. Das Sarma, Non-Abelian quantum order in spin-orbit-coupled semiconductors: Search for topological Majorana particles in solid-state systems, *Phys. Rev. B* **82**, 214509 (2010), arXiv:1006.2829.
- [64] S. B. Chung, H.-J. Zhang, X.-L. Qi, and S.-C. Zhang, Topological superconducting phase and Majorana fermions in half-metal/superconductor heterostructures, *Phys. Rev. B* **84**, 060510 (2011).
- [65] M. Duckheim and P. W. Brouwer, Andreev reflection from noncentrosymmetric superconductors and Majorana bound-state generation in half-metallic ferromagnets, *Phys. Rev. B* **83**, 054513 (2011).
- [66] A. C. Potter and P. A. Lee, Topological superconductivity and Majorana fermions in metallic surface states, *Phys. Rev. B* **85**, 094516 (2012).
- [67] M. Sato, Y. Takahashi, and S. Fujimoto, Non-Abelian topological order in *s*-wave superfluids of ultracold fermionic atoms, *Phys. Rev. Lett.* **103**, 020401 (2009), arXiv:0901.4693.
- [68] C. Zhang, S. Tewari, R. M. Lutchyn, and S. Das Sarma, $p_x + ip_y$ superfluid from *s*-wave interactions of fermionic cold atoms, *Phys. Rev. Lett.* **101**, 160401 (2008).
- [69] A. Vuik, D. Eeltink, A. R. Akhmerov, and M. Wimmer, Effects of the electrostatic environment on the Majorana nanowire devices, *New J. Phys.* **18**, 033013 (2016), arXiv:1511.08044.
- [70] A. E. G. Mikkelsen, P. Kotetes, P. Krogstrup, and K. Flensberg, Hybridization at superconductor-semiconductor interfaces, *Phys. Rev. X* **8**, 031040 (2018).
- [71] G. W. Winkler, D. Varjas, R. Skolasinski, A. A. Soluyanov, M. Troyer, and M. Wimmer, Orbital contributions to the electron *g* factor in semiconductor nanowires, *Phys. Rev. Lett.* **119**, 037701 (2017).
- [72] B. Nijholt and A. R. Akhmerov, Orbital effect of magnetic field on the Majorana phase diagram, *Phys. Rev. B* **93**, 235434 (2016), arXiv:1509.02675.
- [73] S. Schuwalow, N. B. M. Schröter, J. Gukelberger, C. Thomas, V. Strocov, J. Gamble, A. Chikina, M. Caputo, J. Krieger, G. C. Gardner, M. Troyer, G. Aeppli, M. J. Manfra, and P. Krogstrup, Band structure extraction at hybrid narrow-gap semiconductor-metal interfaces, *Advanced Science* **8**, 2003087 (2021).
- [74] P. Chauhan, C. Thomas, T. Lindemann, G. C. Gardner, J. Gukelberger, M. J. Manfra, and N. P. Armitage, Measurements of cyclotron resonance of the interfacial states in strong spin-orbit coupled 2D electron gases proximitized with aluminum, *Appl. Phys. Lett.* **120**, 142105 (2022).
- [75] S. Hart, Z. Cui, G. Ménard, M. Deng, A. E. Antipov, R. M. Lutchyn, P. Krogstrup, C. M. Marcus, and K. A. Moler, Current-phase relations of InAs nanowire Josephson junctions: From interacting to multimode regimes, *Phys. Rev. B* **100**, 064523 (2019).
- [76] A. Kringhøj, G. W. Winkler, T. W. Larsen, D. Sabonis, O. Erlandsson, P. Krogstrup, B. van Heck, K. D. Petersson, and C. M. Marcus, Andreev modes from phase winding in a full-shell nanowire-based transmon, *Phys. Rev. Lett.* **126**, 047701 (2021).
- [77] J. Shen, G. W. Winkler, F. Borsoi, S. Heedt, V. Levajac, J.-Y. Wang, D. van Driel, D. Bouman, S. Gazibegovic, R. L. M. Op Het Veld, D. Car, J. A. Logan, M. Pendharkar, C. J. Palmström, E. P. A. M. Bakkers, L. P. Kouwenhoven, and B. van Heck, Full parity phase diagram of a proximitized nanowire island, *Phys. Rev. B* **104**, 045422 (2021).
- [78] T. Ö. Rosdahl, A. Vuik, M. Kjaergaard, and A. R.

- Akhmerov, Andreev rectifier: A nonlocal conductance signature of topological phase transitions, *Phys. Rev. B* **97**, 045421 (2018), arXiv:1706.08888.
- [79] G. C. Ménard, G. L. R. Anselmetti, E. A. Martinez, D. Puglia, F. K. Malinowski, J. S. Lee, S. Choi, M. Pendharkar, C. J. Palmstrøm, K. Flensberg, C. M. Marcus, L. Casparis, and A. P. Higginbotham, Conductance-matrix symmetries of a three-terminal hybrid device, *Phys. Rev. Lett.* **124**, 036802 (2020).
- [80] D. Puglia, E. A. Martinez, G. C. Ménard, A. Pöschl, S. Gronin, G. C. Gardner, R. Kallaher, M. J. Manfra, C. M. Marcus, A. P. Higginbotham, and L. Casparis, Closing of the induced gap in a hybrid superconductor-semiconductor nanowire, *Phys. Rev. B* **103**, 235201 (2021).
- [81] A. Pöschl, A. Danilenko, D. Sabonis, K. Kristjahan, T. Lindemann, C. Thomas, M. J. Manfra, and C. M. Marcus, Nonlocal conductance spectroscopy of Andreev bound states in gate-defined InAs/Al nanowires (2022), arXiv:2204.02430.
- [82] A. Banerjee, O. Lesser, M. A. Rahman, C. Thomas, T. Wang, M. J. Manfra, E. Berg, Y. Oreg, A. Stern, and C. M. Marcus, Local and nonlocal transport spectroscopy in planar josephson junctions (2022).
- [83] R. Hess, H. F. Legg, D. Loss, and J. Klinovaja, Local and nonlocal quantum transport due to Andreev bound states in finite Rashba nanowires with superconducting and normal sections, *Phys. Rev. B* **104**, 075405 (2021).
- [84] C. Reeg, D. Loss, and J. Klinovaja, Metallization of a Rashba wire by a superconducting layer in the strong-proximity regime, *Phys. Rev. B* **97**, 165425 (2018).
- [85] W. S. Cole, S. Das Sarma, and T. D. Stanescu, Effects of large induced superconducting gap on semiconductor Majorana nanowires, *Phys. Rev. B* **92**, 174511 (2015).
- [86] R. M. Lutchyn, T. D. Stanescu, and S. Das Sarma, Search for Majorana fermions in multiband semiconducting nanowires, *Phys. Rev. Lett.* **106**, 127001 (2011).
- [87] O. Motrunich, K. Damle, and D. A. Huse, Griffiths effects and quantum critical points in dirty superconductors without spin-rotation invariance: One-dimensional examples, *Phys. Rev. B* **63**, 224204 (2001).
- [88] I. A. Gruzberg, N. Read, and S. Vishveshwara, Localization in disordered superconducting wires with broken spin-rotation symmetry, *Phys. Rev. B* **71**, 245124 (2005).
- [89] P. W. Brouwer, M. Duckheim, A. Romito, and F. von Oppen, Topological superconducting phases in disordered quantum wires with strong spin-orbit coupling, *Phys. Rev. B* **84**, 144526 (2011).
- [90] P. W. Brouwer, M. Duckheim, A. Romito, and F. von Oppen, Probability distribution of Majorana end-state energies in disordered wires, *Phys. Rev. Lett.* **107**, 196804 (2011).
- [91] A. M. Lobos, R. M. Lutchyn, and S. Das Sarma, Interplay of disorder and interaction in Majorana quantum wires, *Phys. Rev. Lett.* **109**, 146403 (2012).
- [92] J. D. Sau, S. Tewari, and S. Das Sarma, Experimental and materials considerations for the topological superconducting state in electron- and hole-doped semiconductors: Searching for non-Abelian Majorana modes in 1D nanowires and 2D heterostructures, *Phys. Rev. B* **85**, 064512 (2012).
- [93] W. DeGottardi, D. Sen, and S. Vishveshwara, Majorana fermions in superconducting 1D systems having periodic, quasiperiodic, and disordered potentials, *Phys. Rev. Lett.* **110**, 146404 (2013).
- [94] W. De Gottardi, *Strong correlations and topological order in one-dimensional systems*, Ph.D. thesis, University of Illinois at Urbana-Champaign (2012).
- [95] I. Adagideli, M. Wimmer, and A. Teker, Effects of electron scattering on the topological properties of nanowires: Majorana fermions from disorder and superlattices, *Phys. Rev. B* **89**, 144506 (2014).
- [96] B. Pekerten, A. Teker, O. Bozat, M. Wimmer, and I. Adagideli, Disorder-induced topological transitions in multichannel Majorana wires, *Phys. Rev. B* **95**, 064507 (2017).
- [97] S. Ahn, H. Pan, B. Woods, T. D. Stanescu, and S. Das Sarma, Estimating disorder and its adverse effects in semiconductor Majorana nanowires, *Phys. Rev. Mater.* **5**, 124602 (2021).
- [98] D. Thouless, Localization distance and mean free path in one-dimensional disordered systems, *J Phys. C: Solid State Phys.* **6**, L49 (1973).
- [99] B. D. Woods, S. Das Sarma, and T. D. Stanescu, Charge-impurity effects in hybrid Majorana nanowires, *Phys. Rev. Appl.* **16**, 054053 (2021).
- [100] T. Giamarchi, *Quantum Physics in One Dimension* (Oxford University Press, Oxford, 2004).
- [101] S. Boutin, A. Antipov, W. Cole, J. Gukelberger, F. Karimi, G. Winkler, B. Bauer, and R. Lutchyn, Correlated disorder in one-dimensional topological superconductors (2022), to appear.
- [102] G. Wang, T. Dvir, N. van Loo, G. P. Mazur, S. Gazibegovic, G. Badawy, E. P. A. M. Bakkers, L. P. Kouwenhoven, and G. de Lange, Non-local measurement of quasiparticle distribution in proximitized semiconductor nanowires using quantum dots, arXiv:2110.05373 (2021).
- [103] E. A. Martinez, A. Pöschl, E. B. Hansen, M. A. Y. van de Poll, S. Vaitiekėnas, A. P. Higginbotham, and L. Casparis, Measurement circuit effects in three-terminal electrical transport measurements (2021), arXiv:2104.02671.
- [104] A. Maiani, M. Geier, and K. Flensberg, Conductance-matrix symmetries of multiterminal semiconductor-superconductor devices (2022).
- [105] H. Pan, J. D. Sau, and S. Das Sarma, Three-terminal nonlocal conductance in Majorana nanowires: Distinguishing topological and trivial in realistic systems with disorder and inhomogeneous potential, *Phys. Rev. B* **103**, 014513 (2021).
- [106] A. R. Akhmerov, J. P. Dahlhaus, F. Hassler, M. Wimmer, and C. W. J. Beenakker, Quantized conductance at the Majorana phase transition in a disordered superconducting wire, *Phys. Rev. Lett.* **106**, 057001 (2011).
- [107] A. V. Feshchenko, L. Casparis, I. M. Khaymovich, D. Maradan, O.-P. Saira, M. Palma, M. Meschke, J. P. Pekola, and D. M. Zumbühl, Tunnel-junction thermometry down to millikelvin temperatures, *Phys. Rev. Appl.* **4**, 034001 (2015).
- [108] A. Fornieri, A. M. Whiticar, F. Setiawan, E. Portolés, A. C. C. Drachmann, A. Keselman, S. Gronin, C. Thomas, T. Wang, R. Kallaher, G. C. Gardner, E. Berg, M. J. Manfra, A. Stern, C. M. Marcus, and F. Nichele, Evidence of topological superconductivity in planar Josephson junctions, *Nature* **569**, 89 (2019).
- [109] R. Willett, J. P. Eisenstein, H. L. Störmer, D. C. Tsui,

- A. C. Gossard, and J. H. English, Observation of an even-denominator quantum number in the fractional quantum Hall effect, *Phys. Rev. Lett.* **59**, 1776 (1987).
- [110] W. Pan, J.-S. Xia, V. Shvarts, D. E. Adams, H. L. Stormer, D. C. Tsui, L. N. Pfeiffer, K. W. Baldwin, and K. W. West, Exact quantization of the even-denominator fractional quantum Hall state at $\nu = 5/2$ Landau level filling factor, *Phys. Rev. Lett.* **83**, 3530 (1999), [arXiv:cond-mat/9907356](#).
- [111] A. Kumar, G. A. Csáthy, M. J. Manfra, L. N. Pfeiffer, and K. W. West, Nonconventional odd-denominator fractional quantum Hall states in the second Landau level, *Phys. Rev. Lett.* **105**, 246808 (2010).
- [112] A. A. Zibrov, C. Kometter, H. Zhou, E. M. Spanton, T. Taniguchi, K. Watanabe, M. P. Zaletel, and A. F. Young, Tunable interacting composite fermion phases in a half-filled bilayer-graphene Landau level, *Nature* **549**, 360 (2017).
- [113] L. Fidkowski, R. M. Lutchyn, C. Nayak, and M. P. A. Fisher, Majorana zero modes in one-dimensional quantum wires without long-ranged superconducting order, *Phys. Rev. B* **84**, 195436 (2011), [arXiv:1106.2598](#).
- [114] T. Karzig, C. Knapp, R. M. Lutchyn, P. Bonderson, M. B. Hastings, C. Nayak, J. Alicea, K. Flensberg, S. Plugge, Y. Oreg, C. M. Marcus, and M. H. Freedman, Scalable designs for quasiparticle-poisoning-protected topological quantum computation with Majorana zero modes, *Phys. Rev. B* **95**, 235305 (2017).
- [115] S. Plugge, L. A. Landau, E. Sela, A. Altland, K. Flensberg, and R. Egger, Roadmap to Majorana surface codes, *Phys. Rev. B* **94**, 174514 (2016).
- [116] S. Plugge, A. Rasmussen, R. Egger, and K. Flensberg, Majorana box qubits, *New J. Phys.* **19**, 012001 (2017).
- [117] S. Vijay, T. H. Hsieh, and L. Fu, Majorana fermion surface code for universal quantum computation, *Phys. Rev. X* **5**, 041038 (2015), [arXiv:1504.01724](#).
- [118] S. Vijay and L. Fu, Physical implementation of a Majorana fermion surface code for fault-tolerant quantum computation, *Phys. Scr.* **168**, 014002 (2016), [arXiv:1509.08134](#).
- [119] S. Vijay and L. Fu, Teleportation-based quantum information processing with Majorana zero modes, *Phys. Rev. B* **94**, 235446 (2016), [arXiv:1609.00950](#).
- [120] P. Bonderson, M. Freedman, and C. Nayak, Measurement-only topological quantum computation, *Phys. Rev. Lett.* **101**, 010501 (2008), [arXiv:0802.0279](#).
- [121] P. Bonderson, M. Freedman, and C. Nayak, Measurement-only topological quantum computation via anyonic interferometry, *Ann. Phys.* **324**, 787 (2009), [arXiv:0808.1933](#).
- [122] D. Larocche, S. Das Sarma, G. Gervais, M. P. Lilly, and J. L. Reno, Scattering mechanism in modulation-doped shallow two-dimensional electron gases, *Appl. Phys. Lett.* **96**, 162112 (2010).
- [123] S. Das Sarma and E. H. Hwang, Mobility versus quality in two-dimensional semiconductor structures, *Phys. Rev. B* **90**, 035425 (2014).
- [124] B. Shojaei, A. C. C. Drachmann, M. Pendharkar, D. J. Pennachio, M. P. Echlin, P. G. Callahan, S. Kraemer, T. M. Pollock, C. M. Marcus, and C. J. Palmström, Limits to mobility in InAs quantum wells with nearly lattice-matched barriers, *Phys. Rev. B* **94**, 245306 (2016).
- [125] T. Tschirky, S. Mueller, C. A. Lehner, S. Fält, T. Ihn, K. Ensslin, and W. Wegscheider, Scattering mechanisms of highest-mobility InAs/Al_xGa_{1-x}Sb quantum wells, *Phys. Rev. B* **95**, 115304 (2017).
- [126] A. T. Hatke, T. Wang, C. Thomas, G. C. Gardner, and M. J. Manfra, Mobility in excess of 106 cm²/Vs in InAs quantum wells grown on lattice mismatched InP substrates, *Appl. Phys. Lett.* **111**, 142106 (2017).
- [127] C. Thomas, A. T. Hatke, A. Tuaz, R. Kallaher, T. Wu, T. Wang, R. E. Diaz, G. C. Gardner, M. A. Capano, and M. J. Manfra, High-mobility InAs 2DEGs on GaSb substrates: A platform for mesoscopic quantum transport, *Phys. Rev. Mater.* **2**, 104602 (2018).
- [128] K. S. Wickramasinghe, W. Mayer, J. Yuan, T. Nguyen, L. Jiao, V. Manucharyan, and J. Shabani, Transport properties of near surface InAs two-dimensional heterostructures, *Appl. Phys. Lett.* **113**, 262104 (2018).
- [129] S. J. Pauka, J. D. S. Witt, C. N. Allen, B. Harlech-Jones, A. Jouan, G. C. Gardner, S. Gronin, T. Wang, C. Thomas, M. J. Manfra, J. Gukelberger, J. Gamble, D. J. Reilly, and M. C. Cassidy, Repairing the surface of InAs-based topological heterostructures, *J. Appl. Phys.* **128**, 114301 (2020).
- [130] E. Cimpoiasu, M. J. Fox, B. R. Dunphy, S. Mack, J. A. Christodoulides, and B. R. Bennett, Charge scattering mechanisms in shallow InAs quantum wells, *J. Appl. Phys.* **127**, 145702 (2020).